Evolutionarily conserved fMRI network dynamics in the mouse, macaque, and human brain

Daniel Gutierrez-Barragan[1]*, Julian S.B. Ramirez[2], Stefano Panzeri[3], Ting Xu[4§], Alessandro Gozzi[1*§]

[1]*Functional Neuroimaging Lab, Istituto Italiano di Tecnologia, Center for Neuroscience and Cognitive Systems, Rovereto, Italy*

[2]*Center for the Developing Brain. Child Mind Institute, NY, USA.*

[3]*Department of Excellence for Neural Information Processing, Center for Molecular Neurobiology (ZMNH), University Medical Center Hamburg-Eppendorf (UKE), Hamburg, Germany*

*Correspondence: alessandro.gozzi@iit.it; daniel.gutierrez@iit.it

[§]Share senior authorship

Lead Author:

Alessandro Gozzi PhD
Functional neuroimaging Laboratory
Istituto Italiano di Tecnologia
Center for Neuroscience and Cognitive Systems @ UNITN
Corso Bettini 31, 38068, Rovereto, Italy
alessandro.gozzi@iit.it

ABSTRACT

Evolutionarily relevant networks have been previously described in several mammalian species using time-averaged analyses of fMRI time-series. However, fMRI network activity is highly dynamic and continually evolves over timescales of seconds. Whether the dynamic principles that govern intrinsic fMRI network fluctuations are conserved across mammalian species remains unclear. Using frame-wise clustering of fMRI time-series, we find that fMRI network dynamics in awake macaques and humans is characterized by recurrent transitions between a set of 4 dominant, neuroanatomically homologous fMRI coactivation modes (C-modes), three of which are also plausibly represented in the rodent brain. Importantly, in all species the identified C-modes exhibit species-invariant dynamic features, including intrinsic infraslow dynamics and preferred occurrence at specific phases of global fMRI signal fluctuations. Moreover, C-modes occurrence rates in awake humans, macaques and mice reflect temporal trajectories of least energy and predicts ranking of corresponding functional connectivity gradients. Our results reveal a set of species-invariant principles underlying the dynamic organization of fMRI networks in mammalian species, and offer novel opportunities to relate fMRI network findings across the phylogenetic tree.

INTRODUCTION

Spontaneous fluctuations in resting fMRI signals have been consistently shown to be temporally synchronized across multiple functional systems, delineating a set of reproducible topographies often referred to as Resting State Networks (RSNs)[1,2]. RSN mapping typically entails the computation of time-averaged statistical dependencies between fMRI time-series under the assumption that temporal structure of this activity is time-invariant over a time window of minutes[3]. Prompted by the critical need to complement human fMRI research with mechanistic investigations in physiologically accessible species[4], multiple research group have begun to implement fMRI mapping in non-human primates and rodents[5,6]. These investigations have revealed an interesting set of evolutionary correspondences in the organization of RSN across mammalian species. These include the presence of highly synchronous subcortical and cortical systems, including interhemispheric motor-sensory networks as well as evolutionarily relevant precursors of distributed integrative systems, such as the default mode and salience networks[7–9]. However, spontaneous brain activity is highly dynamic and continuously evolves over the timescale of minutes[10,11]. Accordingly, a large body of experimental and theoretical work has shown that the correlation structure of RSNs is time-varying[12,13], and undergoes dynamic reconfiguration involving transient interactions between distinct functional systems that are continually revisited[14]. These observations suggest that mere time-invariant descriptions of spontaneous fMRI activity are not sufficient to comprehensively describe the functional architecture of the resting brain.

Although many approaches to study the dynamic organization of RSNs have been proposed[12,13], frame-wise methods[15,16] have recently gained traction as a complement to correlation-based approaches. Compared to correlation-based approaches (e.g. sliding-windows analyses), frame-wise methods offer the possibility to (a) temporally localize the peaks and throughs of activity that underlie fMRI network dynamics and relate them to global fluctuations in brain activity, (b) describe the dynamic organization of fMRI in non-correlations terms, using a directly interpretable parameter (i.e. mean BOLD activity), and (c) describe fMRI dynamics using relatively few relevant dimensions, without the need to pre-imposed regional parcellations. Using whole-brain framewise clustering of fMRI time-series to obtain coactivation patterns (CAPs), we and others recently showed that resting fMRI activity is dominated by recurring infraslow network fluctuations encompassing stereotypic brain topographies[15,16]. The simplicity of this framework, its direct association with a directly quantifiable physiological property, as well as its high temporal and spatial resolution are perfectly suited to parsimoniously, yet comprehensively describe the dynamic organization of spontaneous network activity.

While previous studies have compared the static organization of fMRI networks across species[8,17] attempts to relate the dynamic organization of spontaneous activity across the mammalian phylogenetic tree are lacking. Is fMRI network dynamics underpinned by a single set

of species-invariant principles, or does this phenomenon instead reflect unique, species-specific attributes? And does the functional topography of fMRI substates encompass evolutionarily conserved motifs? To address these questions, here, we leveraged fMRI datasets acquired in awake humans, macaques and mice to probe and compare the dynamic organization of fMRI in the mammalian brain. We find that fMRI network dynamics in all probed species is similarly characterized by recurrent transitions between dominant, fMRI "coactivation modes" (C-modes) which exhibit largely conserved topographies and dynamic features. We further expand our findings to relate dynamic states represented by C-modes to principal gradients of the fMRI connectome, thus establishing a link between seemingly independent static and dynamic phenomena. These results suggest that resting fMRI activity in mammalian species is underpinned by evolutionarily conserved dynamic principles.

.

RESULTS

fMRI coactivation modes parsimoniously describe fMRI network dynamics in humans, macaques and mice

To compare the dynamic organization of fMRI network dynamics within an evolutionary perspective, we used a quantitative approach based on the framewise identification of CAPs. This approach entails a clustering of concatenated fMRI volumes across individuals based on their spatial similarity, which are then averaged to produce group-level CAPs[14–16]. Group-level CAP maps are next T-scored at the voxel level, and single-subject CAP maps are obtained by averaging the corresponding clustered frames from each subject (**Figure S1**).

Consistent with prior studies[15], we found that CAPs encompass multiple coactive and anti-coactive pairs with opposite BOLD polarity (**Figure 1**), suggesting a cyclical fluctuation of dynamic states. To capture the cyclical dimension of the CAP and anti-CAP axis and facilitate cross-species comparisons, we here aggregated CAP pairs into coactivation modes (C-modes)[18,19]. Within C-modes, CAP and anti-CAP are regarded as the peak and trough of a fluctuating spatiotemporal pattern. C-modes are then computed by reversing the sign of an anti-CAP and spatially averaging with its paired CAP to spatially depict the corresponding coactivation axis. C-modes thereby describe stereotypic, recurring spatiotemporal patterns of BOLD activity underlying the dynamic organization of resting state fMRI.

CAP (and in turn C-mode) mapping critically depends on the identification of reproducible functional topographies that faithfully explain the observed data. CAPs were extracted within each species with optimal number of clusters that showed the highest reproducibility across individuals and datasets (k = 8, human and macaques, k = 6, mice, see methods section and **Figures S2 and S3**). The employed procedure identified in all species CAPs pairs characterized by similar activation topography but opposite polarity ($R > |0.65|$, all species, all CAP pairs, **Figure 1A-B**). We thus reduced the dimensionality of our analyses by introducing a single spatial representation of CAPs and anti-CAPs to produce 4 (human and macaque) or 3 (mouse) C-modes, respectively (**Figure 1B**). The topography of the individual CAPs pairs that constitute each C-mode is reported in **Figure S4**. To assess the potential confounding contribution of head-motion to C-mode topography mapping, we repeated the clustering procedure on time-series in which we did not scrub fMRI frames exhibiting high motion-related. We next compared the spatial topography of C-modes obtained with and without frame censoring. This comparison revealed virtually indistinguishable maps ($r > 0.95$, all C-modes, all species, **Figure S5A**). Further corroborating a negligible contribution of head motion to our findings, we also found that no C-mode was preferentially enriched with high-motion frames in all species (one-way ANOVA, $p > 0.1$ for all comparisons, **Figure S5B**).

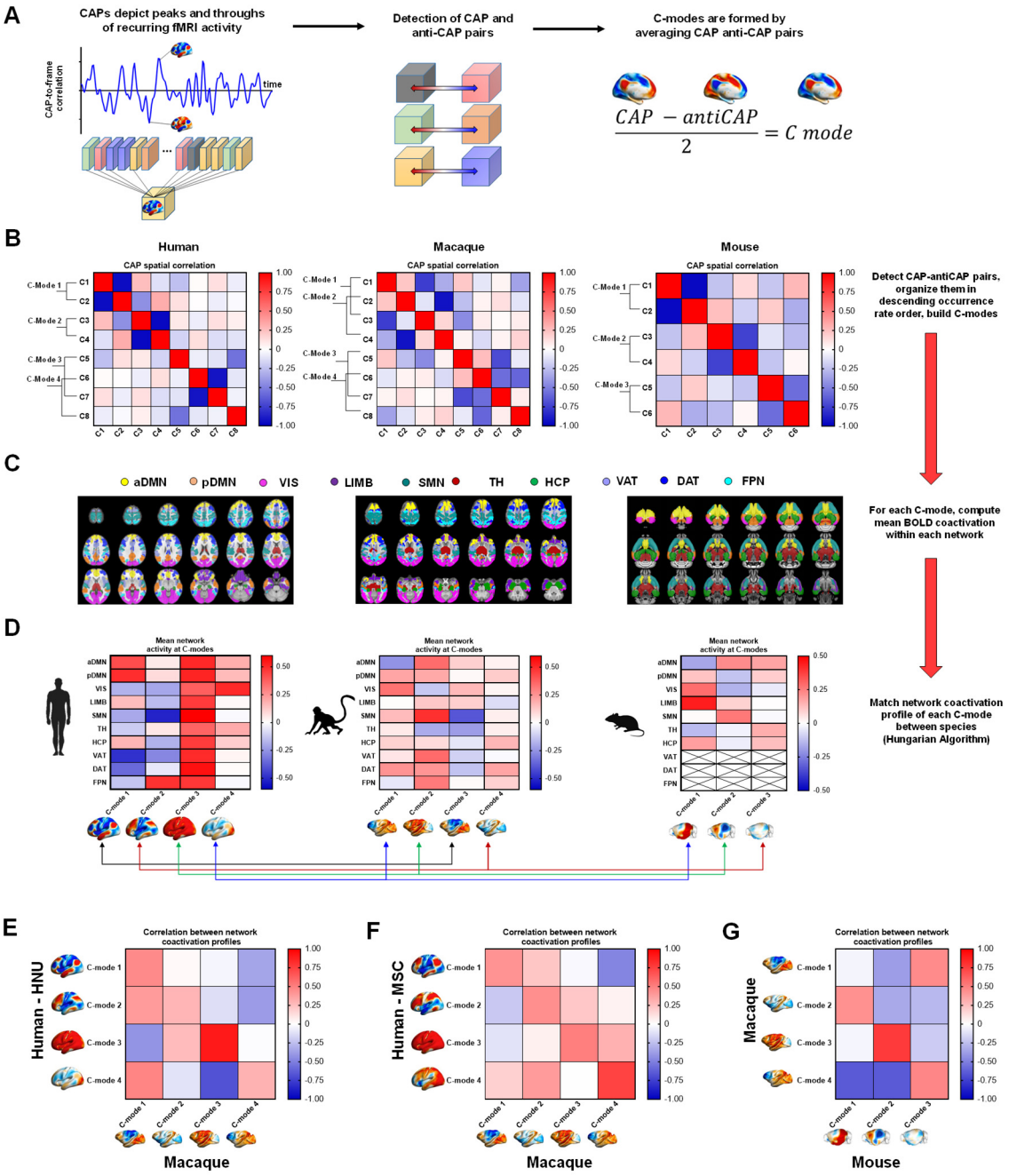

Figure 1. C-mode identification and matching across species (A) CAPs represent transients of infraslow fMRI activity that can be matched in pairs exhibiting opposite polarity (CAPs, anti-CAPs, left). Detection of CAP anti-CAP pairs (middle) allows for the computation of fMRI Coactivation modes (C-modes, right). **(B)** Detection CAP-anti-CAP pairs given highest spatial anticorrelation within the between CAP similarity matrix. The matrix was then organized in descending CAP occurrence rate, and C-modes were built by subtracting the anti-CAP T-score map from the highest recurring corresponding CAP, then dividing by two. **(C)** Evolutionarily relevant fMRI networks used for matching. **(D)** Vectorized network coactivation profiles for each C-mode. Arrows denote matching of C-modes across species performed by the Hungarian Algorithm. **(E)** Correlation between matched C-modes from humans (HNU dataset) and macaques, **(F)** between humans (MSC dataset) and macaques; and **(G)** between macaques and mice. Abbreviations: aDMN - anterior Default Mode; pDMN - Posterior Default Mode; SMN – Somatomotor; VIS – Visual; DAT - Dorsal Attention; VAT- Ventral Attention; FPN – Frontoparietal; LB – Limbic; TH –Thalamus; HC – Hippocampus.

fMRI C-modes exhibit evolutionarily-conserved topographic organization

Having identified representative fMRI C-modes in all three species, we next asked whether the corresponding topographies would show, on top of foreseeable species-specific features, recognizable evolutionarily conserved topographic organization. To address this question, we matched C-modes topography based on the similarity of mean BOLD coactivation profile across a set of evolutionarily conserved resting state networks (RSNs)[20–23] (**Figure 1C-D**) Cross-species C-mode matching was carried pairwise between human and macaque, and between macaque and mouse, respectively, using the Hungarian algorithm. Of note, no anatomical weighting was assigned to frontoparietal, ventral and dorsal attention networks in mice, given the lack of established phylogenetic precursors of these RSNs in the rodent brain[7].

The corresponding matching results are depicted in the form of spatial correlation between network coactivation profiles of human and macaque datasets (HNU and MSC, **Figure 1E and 1F**, respectively), as well as between macaques and mice (**Figure 1G**). Human to macaque matching gave consistent results for both HNU and MSC datasets, with the spatial of topography of human C-modes 1-4 being best aligned to corresponding macaque C-modes 1-4 (see also **Figure 2C**). Because the human HNU dataset included more subjects and was performed at daylight hours as animal scans, we describe our results hereafter for the HNU as main dataset, and present a summary of the obtained MSC results as supplementary figure **(Figure S6).** Macaque to mouse matching linked macaque C-modes 2, 3 and 4 to mouse C-mode 1, 2 and 3, respectively (**Figure 1G, Figure 2C**). Whilst some degeneration was apparent in C-mode matching between single pairs of macaque and mouse C-modes, the chosen algorithmic solution ensured the best network-wise matching across species (**Figure 2C**), as well as preservation of C-mode 3 and 4 phase locking with fMRI global signal cycles (described below, cf. **Figure 4**). As human and macaque C-mode 1 was not preferentially matched to any mouse C-modes, we refer to mouse C-modes as 2, 3, and 4 for consistency throughout the upcoming analyses.

Collectively, cross-species C-mode matching revealed 4 topographically related C-modes in human and macaque, three of which (C-modes 2-4) were also represented in the rodent brain (**Figure 2**). In all species, C-modes exhibited rich spatial organization encompassing positive and negative peaks of BOLD activity that together delineated a set of stereotypic network coactivation profiles (**Figure 2C**, right panels). Specifically, C-mode 1 *(DMN-SMN)* encompassed peaks of BOLD activity in default-mode (DMN) and limbic (LIMB) networks, accompanied by below baseline BOLD activity in somato-motor (SMN) and ventral attention (VAT) areas in both humans and macaques. C-mode 2 (*DMN-Limb*ic) exhibited instead coactivation of DMN areas in anti-correlation with SMN, visual (VIS), and LIMB networks in all three species. C-mode 3 (*SMN-VIS*) activity peaked in the SMN and concomitantly engaged most regions of the human brain, albeit with considerably weaker BOLD activity in visual (VIS) and Thalamic (TH) areas, reminiscent of global fMRI signal (GS) fluctuations. Interestingly, whilst the coactivation profile of SMN-VIS C-mode in macaques and

mice closely recapitulated the human one, fronto-cortical and SMN coactivations in these species were associated with negative (below baseline) VIS and TH activity. Finally, C-mode 4 (*VIS-FPN*) was characterized in humans and macaques by positive coactivation in VIS and posterior cortical regions, and negative coactivation in frontoparietal (FPN) cortical regions. This topography in mouse and macaque, but not humans, was associated with co-deactivation of anterior cingulate and prefrontal regions of the DMN. Taken together, these results point at the presence of topographic correspondences in the organization of C-modes in human, macaque and mouse brains.

Interestingly, while the spatial organization of C-modes exhibited species-invariant topographic features, their occurrence rate showed variation across species (**Figure 2B**). Specifically, in humans we observed a dominant occurrence of DMN-SMN C-mode 1 and 2 ($p < 0.01$, ANOVA) while mice occurrence of sensory-oriented C-mode 3 and 4 was observed instead ($p < 0.01$, ANOVA), with macaques showing equiprobable C-mode occurrence (although a slight trend for a mouse-like profile was apparent). Thus, the temporal structure of C-modes in humans is biased towards a greater occurrence of polymodal integrative metastates (C-modes 1 and 2), with mice, and possibly macaques, exhibiting instead a greater occurrence of sensory-oriented network modes (C-modes 3 and 4).

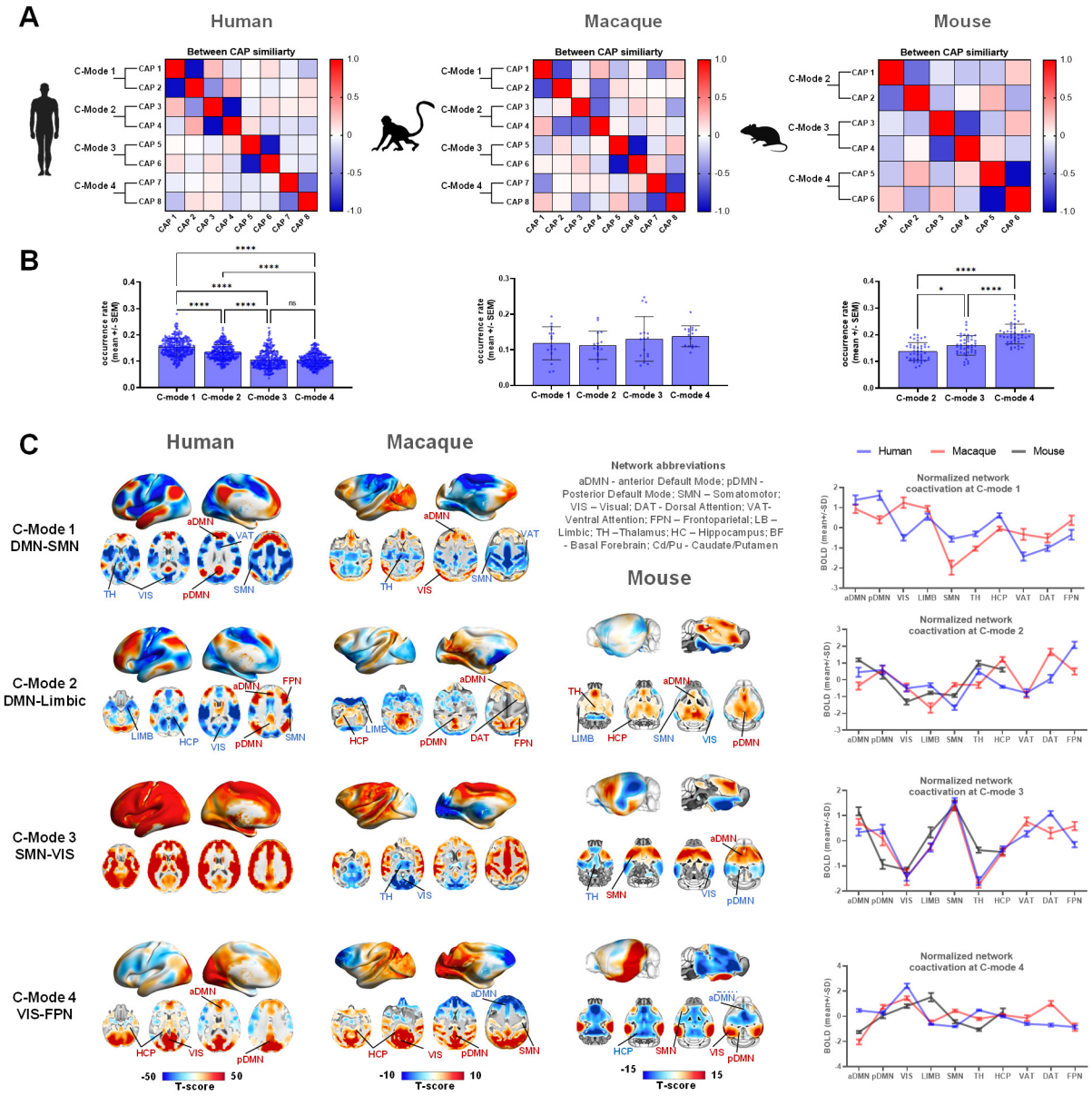

Figure 2. C-mode topography in awake humans, macaques and mice. (A) Between CAP spatial similarity, organized by C-modes. **(B)** C-mode occurrence rates, organized as in (A). **(C)** Topography of C-modes (Left) and corresponding normalized network co-activation profiles (Right, z-scored mean +/- SD of voxels within the network mask). Abbreviations: aDMN - anterior Default Mode; pDMN - Posterior Default Mode; SMN – Somatomotor; VIS – Visual; DAT - Dorsal Attention; VAT-Ventral Attention; FPN – Frontoparietal; LB – Limbic; TH –Thalamus; HC – Hippocampus; BF - Basal Forebrain; Cd/Pu - Caudate/Putamen.

fMRI C-modes exhibit infraslow dynamics in humans, macaques and mice

Previous investigations in awake and anesthetized mice revealed that CAPs undergo infraslow (< 0.04 Hz) fluctuations[15,22]. We thus tested whether C-modes in humans and macaques would be analogously characterized by infraslow dynamics by computing, at each instant of time, a C-mode-to-frame correlation time-series (hereafter referred to as "C-mode time-courses") for each subject/animal. The ensuing power spectra revealed that the temporal evolution of C-mode activity peaked in the infraslow (0.01-0.03 Hz) frequency band in all species (**Figure 3**). Peaks of infraslow activity were distinct and sharp in humans, and slightly less prominent (but clearly recognizable) in mice and macaques. We next investigated the assembly of each C-mode by normalizing its time-course and by time locking event-kernels at the group level. This analysis revealed that C-modes in awake humans, macaques and mice assemble and disassemble in a slow and gradual fashion (**Figure 3**, red insets). These results suggest that the fMRI C-modes exhibit evolutionarily conserved infraslow dynamics across mammalian species.

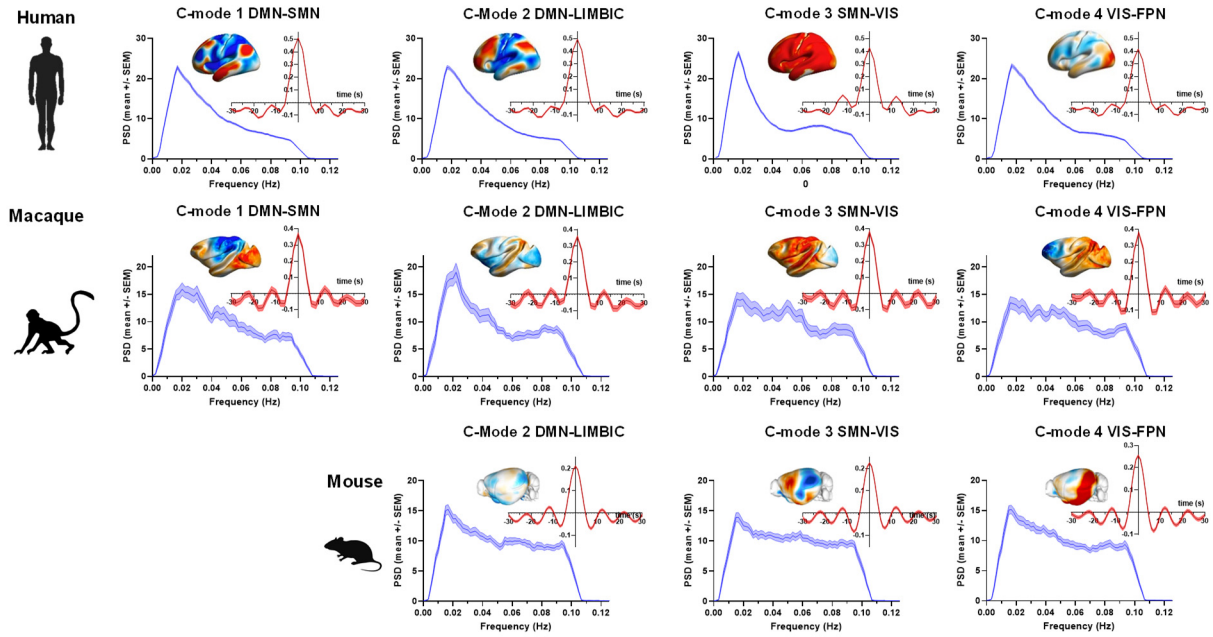

Figure 3. Infraslow dynamics and formation of C-Modes. Group-level power spectral density (blue, mean+/- SEM) of C-Mode to fMRI frame correlation time-series. Red insets denote the mean+/- SEM correlation values time-locked to peaks in the C-Mode time-series.

fMRI C-modes occur at specific phase of fMRI global signals cycles in humans, macaques and mice

Prompted by previous investigations in mice[22], we next probed if C-modes have a preferred occurrence within Global fMRI Signal (GS) cycles in all species. To this purpose, we first ascertained that also in awake conditions the fMRI global signal would dominantly fluctuate within the infraslow range in all species (**Figure 4A**). A spectral analysis showed that the power spectrum of GS sharply peaks within a 0.01-0.03 Hz band in awake humans, with analogous (albeit less

pronounced) peaks of activity in the same frequency range in both awake macaques and mice. Importantly, C-mode occurrence was significantly phase-locked within GS cycles in humans, macaque and mice, suggesting that coupling of C-mode occurrence to intrinsic GS fluctuations is a key organizational principles of fMRI dynamics in multiple mammalians species, independent of their evolutionarily complexity (**Figure 4B**, Rayleigh test, $p < 0.05$, FDR corrected). Moreover, GS-phase distributions in macaques and humans presented notable similarities, with C-modes 1, 3 and 4 (but not 2) exhibiting remarkably conserved cross-species phase alignment. Moreover, C-modes 3 and 4 showed broadly similar circular means across all the three species examined here.

Finally, we investigated whether C-modes were phase-coupled within GS cycles. We computed the GS phase difference between the occurrences of two C-modes within the same cycle, or its immediately adjacent ones (**Figure S7**). These analyses revealed highly consistent positioning of a C-mode within each GS cycle (**Figure S7**, diagonals) and phase coupling between some C-mode pairs (see C-mode 2 and 3 and 3 and 4 in humans, and C-modes 3 and 4 in mice). These results suggest that in mammalian species intrinsic fMRI signal fluctuations do not reflect spatially undifferentiated peaks and troughs of BOLD activity, but instead encompass infraslow cycling between stereotyped coordinated patterns of activity[15]. This general principle can be extended to entail the evolutionary conservation of the phase-relationship with fMRI GS cycles for most (albeit not all, see C-mode 2) of the explored C-modes.

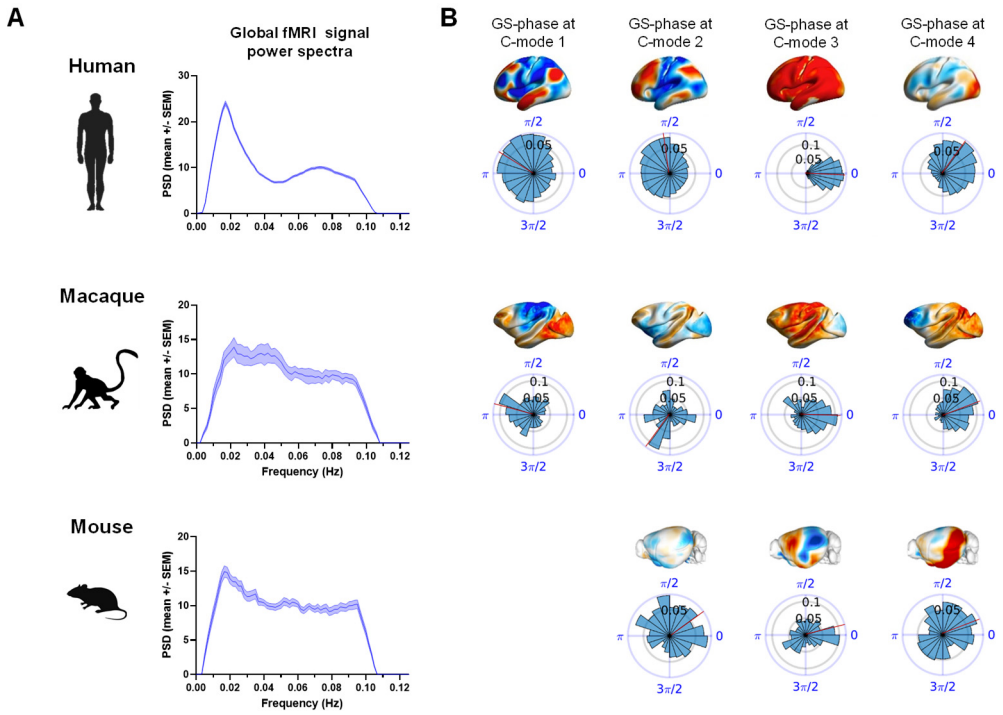

Figure 4. C-mode occurrence within fMRI global signal infraslow cycles. (A) Group-level power spectral density (mean+/- SEM) of the GS. **(B)** Distribution of GS-phases at the occurrence of each C-mode. Red-radial lines denote the circular mean of the distributions, which significantly deviate from circular uniformity (Rayleigh test, $p < 0.05$, FDR corrected).

C-modes occurrence rates reflect temporal trajectories of least energy in human, macaques and mice

We next considered whether the temporal structure of C-mode transition could similarly be underpinned by species-invariant principles. We modeled the system as a Markov process and we computed the transition probability into a different C-mode, as well as C-mode self-transitions (also termed persistence probability, **Figure 5A**). We found that the most recurring C-modes (C-modes 1-2, 3-4, and 3-4 in humans, macaques, and mice respectively) were sinks of preferred directional transitions ($p < 0.01$, red crosses in **Figure 5A**). Furthermore, we investigated, for each species, the "accessibility" of C-modes from one other by computing the corresponding Entropy of Markov Trajectories (HMT)[24] of the transition probability matrices. The HMT measures the complexity of a transition: low descriptive complexity (near-zero HMT) from an initial C-mode to its destination implies an almost deterministic direct path or high accessibility. On the contrary, high HMT values suggest high uncertainty, requiring random steps through different C-modes before reaching the destination, i.e. low accessibility.

In keeping with the C-mode occurrence rate we describe in **Figure 2**, the most recurring C-modes in all species were also those that were most accessible (**Figure 5B**). We further quantified this phenomenon by adding, at the single-subject level, the elements of each column in the HMT matrix and comparing the summative complexity of reaching a specific C-mode (one-way ANOVA, and Tukey test, **Figure 5C**). We found that in humans, C-modes 1 and 2 are the most accessible ones ($p < 0.0001$ against C-modes 3-4). In macaques we did not find any C-mode to have preferred accessibility ($p = 0.25$). Conversely, in mice, C-modes 2 and 3 were the most accessible ones ($p < 0.0001$). Importantly, in all species the ensuing accessibility profile (**Figure 5C**) recapitulated the C-mode occurrence rates we described in **Figure 2B,** with the most accessible C-modes being also the most occurring ones (**Figure 2B**). These findings suggest that C-modes occurrence reflects temporal trajectories of least energy in human, macaques and mice.

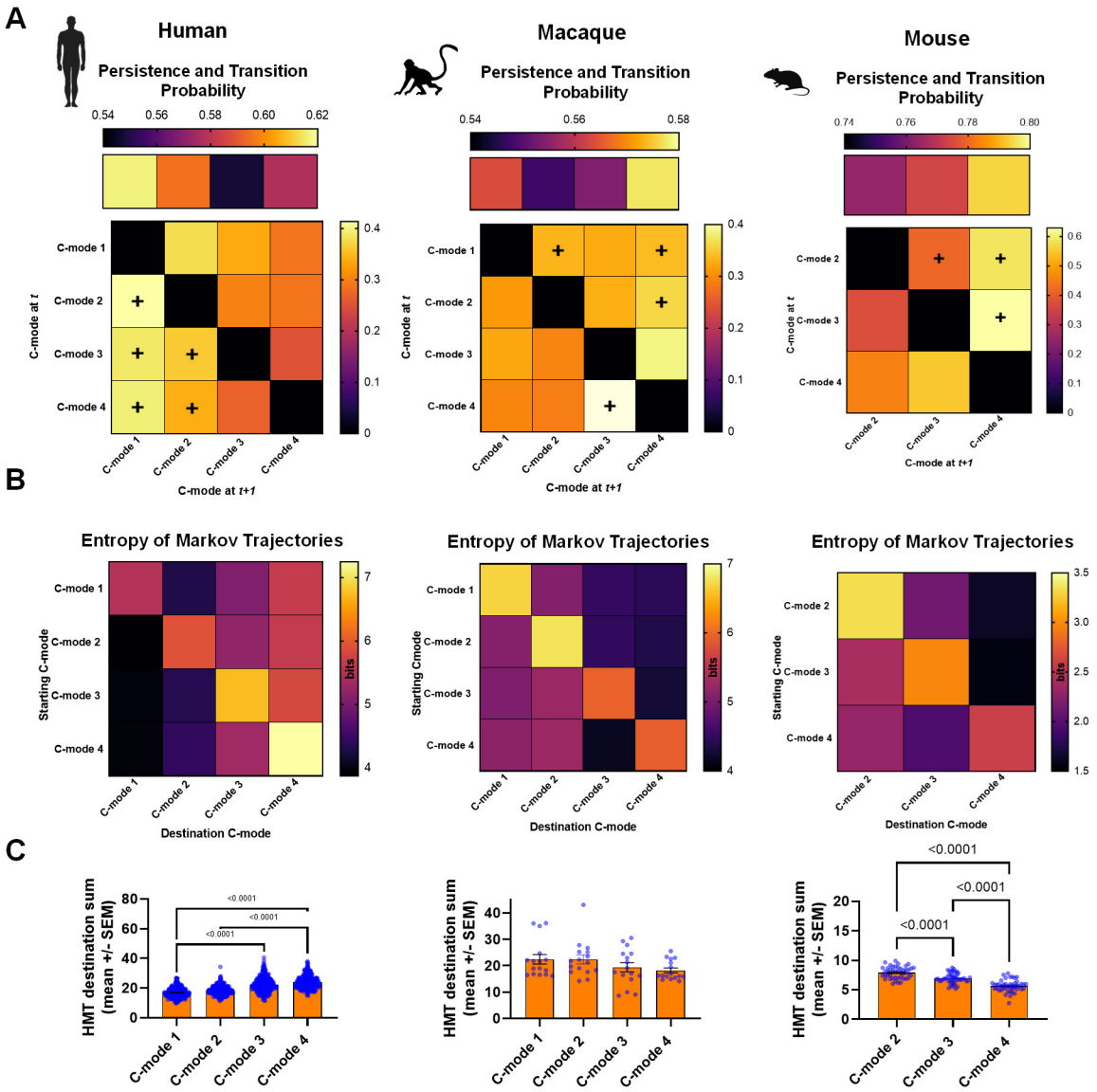

Figure 5. Temporal trajectories of C-modes converge to the most recurring state. (A) Persistence (top row) and transition (off-diagonal) probability in human (left), macaques (middle), and mice (right). Red crosses denote the destination C-mode of preferred directional transitions (Pij > Pji). **(B)** Entropy of Markov trajectories (HMT) show that the C-mode with the highest accessibility are C-modes with higher occurrence rates (i.e. C-mode 1 in humans, and C-mode 4 in macaques and mice). Higher entropy indicates lower accessibility of a destination C-mode (column) from a starting C-mode(row). **(C)** Quantification of the sum of Entropy of Markov Trajectories for all destinations (columns in the HMT matrices at the single-subject level), and comparison between the means (one-way ANOVA, and Tukey test for multiple comparisons $p < 0.05$). The most occurring C-modes (cf **Figure 2**) are also the most accessible ones.

fMRI C-mode occurrence predicts ranking of functional connectivity gradients in humans, macaques and mice

A high portion of the variance in static fMRI connectivity is explained by a limited fraction of fMRI frames exhibiting exceedingly high cofluctuation amplitude[15,25,26]. We thus investigated whether the dynamic occurrence of C-modes could play a critical role in shaping the static functional connectome. In keeping with this (**Figure S7A**), we found that in all species, the weighted average by occurrence rate of C-mode co-fluctuation matrices exhibited high correlation with the corresponding group-mean static functional connectivity matrix ($r > 0.57$, all species, with $r = 0.75$ in humans). These findings suggests that the spatiotemporal patterns of fMRI activity described by C-modes serve as key constituents of static functional connectomes

Prompted by these result, we next asked whether C-mode dynamics could influence (or be related to) the organization of fMRI connectivity gradients[17,27]. Specifically, we posited that C-mode occurrence rate may determine the ranking of functional connectivity gradients, with dominant (i.e. most occurring) C-modes aligning with the gradients that explain the most variation in fMRI connectivity. We thus first computed for each species the first five fMRI connectivity gradients, and next ranked them by decreasing variance explained (**Figure S8**). We then compared, for each species, the spatial similarity of the obtained gradients to that of each C-mode, matching them according to their highest absolute spatial correlation. Plausible spatial correspondences between C-mode and gradient topographies were observed in all species (**Figure 6A**). Corroborating our initial hypothesis, in humans the most occurring C-modes 1 and 2 were matched with dominant gradients 1 and 2, while in macaques and mice dominant gradients 1 and 2 were matched with most occurring C-modes 4 and 3. Moreover, in all species C-mode occurrence was linearly related to the variance explained by each gradient ($R^2 > 0.78$ for all species, **Figure 6B**). These findings suggests that C-modes, and their relative occurrence rate, critically shape the organization of the static fMRI connectome as well as the variance explained by its principal gradients in all the probed mammalian species.

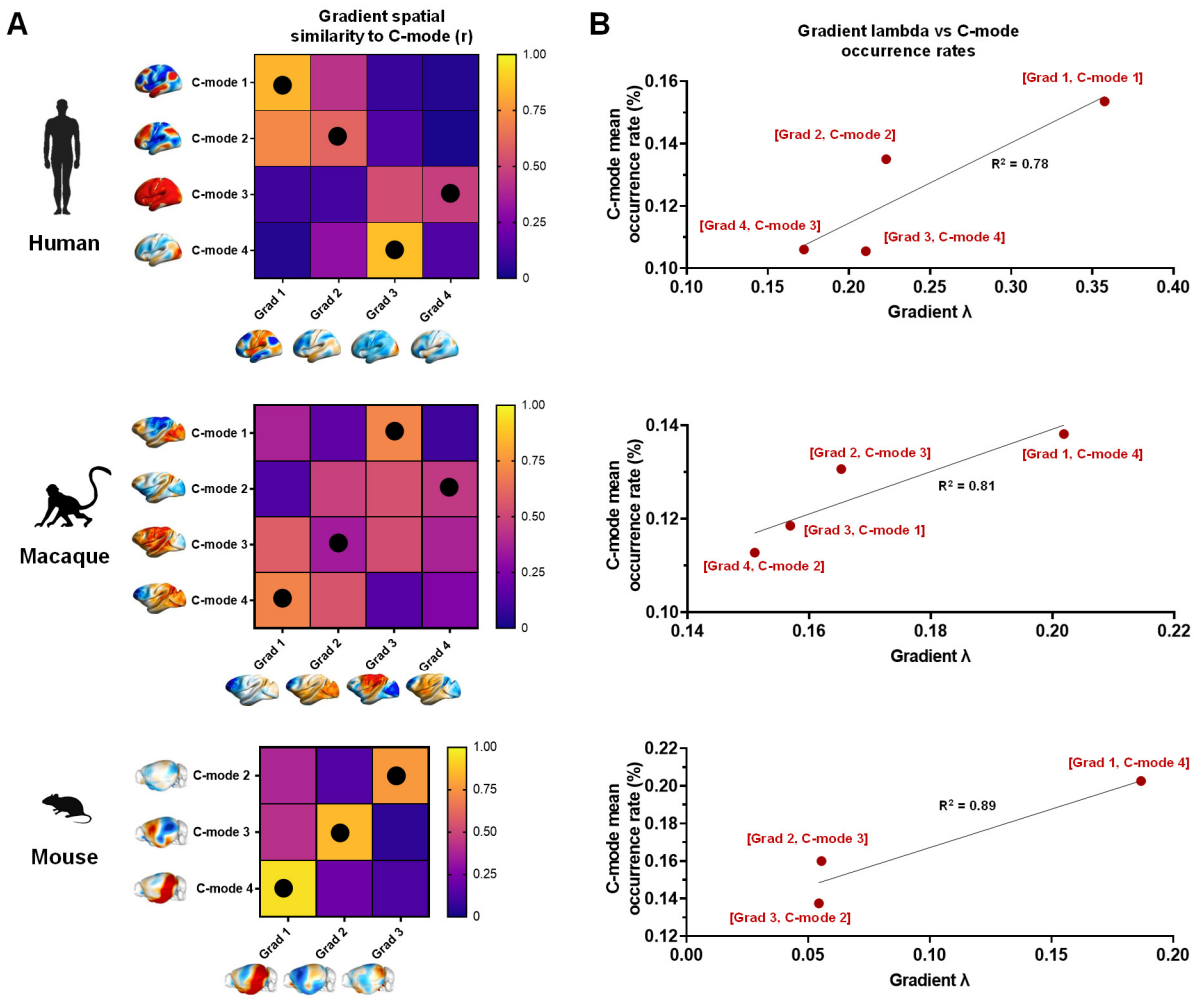

Figure 6. C-modes occurrence rate predicts ranking of functional connectivity gradients. (A) Spatial correlation between the principal gradients and each C-mode map. Black dots denote the spatial matching between maps obtained using the Hungarian Algorithm. **(B)** Scatter plot of the variance explained by each gradient (lambda) versus the corresponding C-mode occurrence rate. R-square from a linear fit ($p < 0.01$). The most occurring C-modes accounts for most variance in the corresponding gradient axis.

DISCUSSION

While previous cross-species studies have attempted to compare the static functional architecture of specific fMRI networks via time-invariant fMRI connectivity mapping[7,28,29], whether the dynamic organization of intrinsic fMRI activity is evolutionarily conserved remains unclear. To fill this knowledge gap, we performed a first-of-its-kind systematic investigation of intrinsic fMRI dynamics in awake humans, macaques and mice using the same analytical framework. To facilitate cross-species comparisons, we introduced a parsimonious description of network dynamics via fMRI C-modes, which were here defined as a spatially averaged CAP anti-CAP pairs. Using this simple approach, we found that fMRI dynamics in awake humans, macaques and mice encompasses the recurring occurrence of a dominant set of neuroanatomically homologous C-mode topographies. We also report that the dynamic structure of fMRI network activity follows a set of evolutionarily-invariant principles. These include the observation that C-modes fluctuate predominantly in the infraslow range, occur at specific phases of the global fMRI signal, and have preferential transitions towards the most recurring C-mode. Moreover, their occurrence rates reflect temporal trajectories of least energy and predict ranking of corresponding functional connectivity gradients. These observations suggest that, beyond and above a number of expected species-specific features, the dynamic structure of fMRI network dynamics in the awake mammalian brain is evolutionarily conserved.

The lack of systematic comparisons of the dynamic organization of fMRI activity across species does not allow us to directly relate our findings to prior literature. However, many of our results are consistent with emerging evidence supporting the presence of cross species correspondences in topography of fMRI network systems of the mammalian brain[23,30] and the close link between the dynamic organization of fMRI, and its steady-state architecture as probed with measures of static functional connectivity[13,22,25]. In the current study, we document that a limited set of neuroanatomically homologous network interactions, represented by C-modes, dominates variance in mouse, macaque and human datasets. Importantly, the topographic organization of C-modes delineates multiple large-scale network systems previously described in multiple mammalian species, including the DMN, salience and motor-sensory network, along with many key subcortical systems[9,20,22]. Extending previous observations[22,31,32], we also found that C-mode-based cofluctuation matrices reliably reconstitute the static organization of the fMRI connectome in all the probed species. These results reconcile findings from prior studies describing the dynamic structure of fMRI connectivity in rodents[15,33–35], macaques[36], and humans[14,16,18,37–40] by establishing a simple framework linking the dynamic organization of fMRI activity to its steady-state architecture. These results are also in agreement with the assumption that the mechanisms underlying interareal communication as assessed with fMRI are conserved in the mammalian brain[41,42].

Our observation that the dynamic structure of fMRI activity in mammals follows species-invariant principles is an important finding, because many fundamental physiological and anatomical features (including the brain's anatomical architecture), have been instead shown to scale with body size, or to be only marginally represented in lower species[43–45]. Our results thus suggest that, independent of evolutionary complexity, a few dominant and highly structured spatiotemporal patterns of infraslow fMRI activity similarly underpin the organization of spontaneous network activity in multiple mammalian species. In this respect, one important advancement of the present study is the use of datasets collected in awake conditions in all species, an experimental strategy that allowed us to carry out a cross-species comparison of the dynamic organization of fMRI activity unconfounded by the pharmacological effects (and the ensuing brain state changes) produced by anesthesia. An additional key benefit of the C-mode framework we introduce here is computational tractability, which allows for the representation of the corresponding spatiotemporal patterns of fMRI activity with voxel resolution (i.e. without predefined anatomical boundaries) and avoiding the use of correlation-based metrics (e.g. like in sliding window-based dynamic connectivity mapping). Moreover, the employed approach allows for a fine-grained temporal localization of dynamic effects with single-frame resolution. All of these properties were key to the identification of the dynamic properties and cross-species correspondences we report in this work.

The voxelwise topography of C-modes enabled us to match and compare these spatiotemporal patterns at maximum spatial resolution, revealing a set of anatomically related motifs that were conserved across species. Cross-species correspondences were more pronounced between human and macaque, where 4 neuroanatomically homologous C-modes could be plausibly identified using two independent human datasets. Not surprisingly, macaque to mouse matching exhibited higher putative degeneracy, an expected finding given the larger phylogenetic distance between these two species. While the C-mode matching strategy we employed preserved fMRI polarity in key anchor networks and reconstituted conserved C-mode GS phase coupling in macaques and mice, more refined matching may be obtained in future studies by incorporating data from lissenchephalic new world monkeys, and other primate species phylogenetically closer to rodents that could serve as intermediate evolutionary link between macaques and mice[5,46,47]. This approach may represents a warranted extension of our work, owing to the increased availability of fMRI data in multiple primate species[5].

The observation of a substantial coupling between C-mode occurrence and cycles of fMRI global signal is an interesting result that we initially reported in anesthetized mice[15], and which we extend here to awake humans and macaques. This finding corroborates the hypothesis that fluctuations in fMRI GS, when devoid of artefactual contaminations, are the manifestation of highly structure network interactions[48].In the light of the accumulating evidence linking intrinsic fluctuations in arousal with fMRI global activity[18,49–51] this finding also suggests that C-modes, as

well as their spatiotemporal BOLD correlates obtained within different computational frameworks[18,25], could be sculpted by (or even the result of) intrinsic input of ascending modulatory systems. Within this framework, differences in arousal state between human and awake animal recordings may putatively be invoked to explain the different coactivation profile observed for C-mode 3 (SMN-VIS). In humans this C-mode showed extended coactivation of most of the cortex, with lower BOLD signal peaks in visual and thalamic areas, while in macaques and mice these areas exhibited larger BOLD signal differences, with opposite polarity to frontocortical regions. As this C-mode is tightly locked to peaks of global fMRI signal activity, the more extended coactivation observed in humans may reflect relatively lower arousal states of compliant human subjects, compared to that of scanner-habituated animals. This notion would be consistent with evidence of an inverse relationship between arousal or vigilance and global fMRI activity[49], and with experimental data in mice, in which the use of anesthesia (and the ensuing low arousal state), was associated with CAPs recapitulating the pancortical profile observed in humans[15].

While the present work focuses on the description of species-invariant principles underling the organization of spontaneous fMRI activity, species-specific features were also apparent. Beyond foreseeable discrepancies in the topography of specific C-modes, which can be related to the increased complexity of the cortical mantle across the phylogenetic tree, one interesting difference we observed is a shift in C-mode occurrence across species. Although comparable human C-modes were identified in macaques and mice, their occurrence rate was inversed, with C-modes 1-2 being the most occurring patterns in humans and C-modes 3-4 in mice and in macaques. Taken together, these observations support the evolutionary basis for ongoing dynamic changes across species, albeit with a shift in the time that each species spends in each spatiotemporal state. Such species-dependent shift in C-mode occurrence may reflect brain adaptations that support the increasing demands of higher-order cognition throughout evolution. As BOLD activity profiles activity in C-modes 1-2 and 3-4 peak in polymodal and sensory areas, respectively, this finding also suggests that in humans the intrinsic organization of fMRI activity is biased towards introspective states that are less frequently visited in animals. Accordingly, we found that these most recurrent C-modes are also the most easily accessible from any other C-mode. Our results also highlight a link between the dynamic organization of fMRI activity and the principal axis of variance of static fMRI activity as mapped with functional connectivity gradients. This result suggests that the macroscale organization of the functional connectome is critically shaped by the occurrence of its constituting spatiotemporal modes, a notion supported also by complementary conceptualization of fMRI dynamics[52].

In summary, we describe a conserved set of dynamic rules governing large-scale fMRI network dynamics in human, macaques and mice. Our work provides a simple and flexible framework to quantitatively model intrinsic fMRI dynamics and relate fMRI network organization across the phylogenetic tree.

MATERIALS AND METHODS

Data and preprocessing

Resting state fMRI (rsfMRI) datasets from awake, freely breathing humans, macaques, and mice were used in this study. Preprocessing included most steps suggested by the guidelines of the Human Connectome Project[53], using a combination of fMRI dedicated software AFNI[54], FSL[55], FreeSurfer[56], and SPM12 (http://fil.ion.ucl.ac.uk/spm/).

Human

The main dataset, Hangzhou Normal University of the Consortium for Reliability and Reproducibility (CoRR-HNU, or HNU)[57] includes 10 sessions of 10-min scans over the course of a month from n = 30 young healthy adults with no history of neurological or psychiatric disorders, head injuries, nor substance abuse (balanced sexes, age = 24+/- 2.41 years). Before scanning, participants were asked to relax and remain still with their eyes opened, avoiding falling asleep. During scanning, a black crosshair was shown in the middle of a grey background. The study was approved by the ethics committee of the Center for Cognition and Brain Disorders at Hangzhou Normal University, and all participants signed written consent before data collection. A GE MR750 3T scanner (GE Medical Systems, Waukesha, WI, USA) was used to acquire MRI data. Functional scans were acquired with an echo-planar imaging sequence - EPI: TR = 2 s, TE = 30 ms, flip angle = 90°, FOV = 220 × 220 mm, matrix = 64 × 64, voxel-size = 3.4 mm isotropic, 43 slices. Data was downloaded from the International Neuroimaging Data-Sharing Initiative (INDI - http://fcon_1000.projects.nitrc.org/indi/CoRR/).

The Midnight Scan Club (MSC) dataset[58] was used as secondary, replication dataset. Five out of 10 randomly selected sessions were used from separate days, and included 30-min scans from n = 10 healthy young adults (balanced sexes, age = 29.1 +/- 3.3 years). Participants were asked to visually fix on a white crosshair against a black background. The study was approved by the Washington University School of Medicine Human Studies Committee and Institutional review Board, and all participants signed written consent before scanning. Functional scans were acquired with a Siemens TRIO 3T MRI scanned (Erlangen, Germany) using a gradient-echo EPI sequence: TR = 2.2 s, TE = 27 ms, flip angle = 90°, voxel-size = 4 mm isotropic, 36 slices. Data was downloaded from OpenNeuro (doi:10.18112/openneuro.ds000224.v1.0.3).

Preprocessing. The first 5 fMRI volumes were removed from each subject's raw data, then despiking (AFNI *3dDespike*) and slice-timing correction (AFNI *3dTshift*) was performed. Data subsequently underwent motion-correction (AFNI *3dvolreg*); skull-stripping (FSL *fast* and *bet*[59]); co-registration to the MNI 3 mm isotropic template (FSL *flirt*); regression of nuisance parameters (white matter, cerebrospinal fluid, and 24 motion parameters (6 parameters, 6 derivatives, and their respective squared time-series) (AFNI *3dDeconvolve*); band-pass filtering between 0.01-0.1

Hz (AFNI *3dBandpass*); spatial smoothing with a 6 mm FWHM kernel (AFNI *3dBlurInMask*); and voxel time-series were finally normalized to z-scores (zero-mean, and standard deviation units).

Macaque

The Newcastle dataset (NC) includes n = 14 rhesus macaque monkeys (*Macaca Mulatta*) scanned with no contrast agents, from which N = 10 animals (2 females, 8 males), in which two independent fMRI session were available, were used for our analyses (age = 2.28 +/- 2.33, weight = 11.76 +/- 3.38). Two additional animals were discarded from our analyses due to excessive head motion. Animal procedures, head-fixation, and protocols were approved by the UK Home Office and comply with the Animal Scientific Procedures Act (1986) on the care and use of animals in research and with the European Directive on the protection of animals used in research (2010/63/EU) (see Slater et al., 2016 for protocol specifics on animal preparation for awake imaging[60]). A Vertical Bruker 4.7T primate dedicated scanner was used and rsfMRI experiments were performed in awake, head-fixed animals for two separate sessions with TR = 2 s; TE = 16 ms, voxel-size = 1.2 mm isotropic. Data was downloaded from NHP data sharing consortium PRIME-DE (http://fcon_1000.projects.nitrc.org/indi/indiPRIME.html)[61].

Preprocessing. The first 5 rsfMRI volumes were removed from each animal's raw data, then despiking (AFNI *3dDespike*) and slice-timing correction (AFNI *3dTshift*) was performed. Data subsequently underwent motion-correction (AFNI *3dvolreg*); skull-stripping (FSL *fast* and *bet*[59]); co-registration to the Yerkes19 2 mm isotropic template[62] (FSL *flirt*); regression of nuisance parameters (white matter, cerebrospinal fluid, and 24 motion parameters (6 parameters, 6 derivatives, and their respective squared time-series) (AFNI *3dDeconvolve*); band-pass filtering between 0.01-0.1 Hz (AFNI *3dBandpass*); spatial smoothing with a 3 mm FWHM kernel (AFNI *3dBlurInMask*); and voxel time-series were finally normalized to z-scores (zero-mean, and standard deviation units).

Mouse

C57BL/6J mouse data was obtained from n = 44, head-fixed awake male mice undergoing a 12-min rsfMRI scan using the same animal preparation, habituation and scanning protocols previously described[22]. *In vivo* experiments were conducted in accordance with the Italian law (DL 26/214, EU 63/2010, Ministero della Sanita, Roma) and with the National Institute of Health recommendations for the care and use of laboratory animals. The animal research protocols for this study were reviewed and approved by the Italian Ministry of Health and the animal care committee of Istituto Italiano di Tecnologia (IIT). All surgeries were performed under anesthesia. Young adult (< 12 months old) male C57BL/6J mice were used. RsfMRI scans, both retrieved and newly acquired, were acquired at the IIT laboratory in Rovereto (Italy) using a Bruker 7T scanner (Bruker Biospin, Ettlingen) with a BGA-9 gradient set, 72 mm birdcage transmit coil, and a four-

channel solenoid receiver coil: TR = 1 s, TE = 15 ms, flip angle = 60°, matrix = 100 × 100, FOV = 2.3 × 2.3 cm, 18 coronal slices 0.6 mm thick, 12 minutes total acquisition time.

Preprocessing. The first 120 rsfMRI volumes (2-min) were removed from each animal's raw data to account for thermal gradient equilibration, then despiking (AFNI *3dDespike*) was performed. Due to the short TR we did not perform slice-timing correction in these images. Data subsequently underwent motion-correction (FSL *mcflirt*); skull-stripping (FSL *fast* and *bet*[59]); co-registration to an in-house mouse brain template of 0.23 × 0.23 × 0.6 mm^3 (ANTS registration suite[63]); regression of nuisance parameters (white matter, cerebrospinal fluid, and 24 motion parameters (6 parameters, 6 derivatives, and their respective squared time-series) (AFNI *3dDeconvolve*); band-pass filtering between 0.01-0.1 Hz (AFNI *3dBandpass*); spatial smoothing with a 0.5 mm FWHM kernel (AFNI *3dBlurInMask*); and voxel time-series were finally normalized to z-scores (zero-mean, and standard deviation units).

Whole brain CAP detection and cluster-number selection

To identify recurrent rsfMRI whole-brain states, we used the whole-brain coactivation patterns (CAPs) approach[14–16] in which fMRI frames are cluster based on their spatial similarity and then averaged to define recurrent patterns of BOLD coactivation. Specifically, for each species, we first performed censoring of motion-contaminated frames (framewise Displacement: FD > 0.3, 0.3, and 0.075 mm for humans[2], macaques[21], and mice[22] respectively), and then concatenated the frames from all subjects or animals. Given that clustering human fMRI data in the 3 mm MNI-space became computationally challenging owing to its large dimensionality (n-voxels = 43.539, compared to 11.402 in macaques, and 8.937 in mice), this step was carried out upon reducing data using the coarse 950-ROI Craddock Parcellation[64]. The choice of this specific parcellation regards its ability to provide a fair dimensionality reduction, while preserving information present at the voxel scale[64]. After these final steps, we ran, for each species, the k-means clustering algorithm[15,65] (spatial correlation as distance metric, 500 iterations, 5 replications with different random initializations, from k = 2:20, 5 independent runs). CAP maps were obtained at the group level by averaging the fMRI frames belonging to a cluster at the voxel level, then normalizing these values to T-scores from the concatenated datasets **(Figure S1)**. At the single-subject level, we obtained, for each subject/animal, a CAP-map for each cluster by only averaging and converting to T-scores, the frames belonging to a cluster but only within a subject/animal's data/session. We note that CAP mapping through frame averaging in humans was done at the voxel level, as the parcellated data was only used for clustering purposes. After clustering, we recovered the censored fMRI frames to the cropped datasets and assigned them to the CAP with the highest spatial correlation. This was done in order to have a continuum of frames for subsequent analyses.

Selection of the optimal number of clusters was done following a set of previously proposed empirical rules[15,40], as well as new metrics. These were dependent on the availability on test-retest

sessions within a dataset in macaques and humans, as well as a full independent dataset in humans from a different site. Specifically, for human HNU and MSC datasets independently, we first ran the k-means clustering algorithm with the concatenated dataset from k = 2:20, selecting, for each 'k', the solution with the highest variance explained[15] from 5 replications in 5 independent runs. For each dataset independently, we first computed the variance explained by data partitioned into an increasing number of clusters ($2 \leq k \leq 20$) (**Figure S2A-B**). We next assessed the topographic consistency of CAPs at increasing partitions. To this purpose, we computed how consistent CAPs are by assessing, for each 'k' partition, the spatial correlation between a mean CAP map, and its matched map in the previous order (k-1) partition. Matching was done using the Hungarian Algorithm[66]. This analysis revealed that partitions between k = 6:10 yielded, in both datasets, topographically stable CAPs that could be reliably identified at higher 'k' (**Figure S2C-D**).

We then assessed the within-dataset repeatability by comparing the spatial correlations between the mean CAP maps of each subject between each independent fMRI sessions (10 for HNU, and 5 for MSC, **Figure S2E-F**). Statistical significance of the mean within subject repeatability of each CAP was assessed by recomputing the spatial correlations between subject-level CAP maps after randomly shuffling the CAP-identity of fMRI frames, preserving occurrence rates. This process was repeated 1000 times, and repeatability values for each subject beneath the highest permutation value were flagged as non-repeatable (asterisks in **Figure S2E-F**). The result of these comparisons showed that within an upper limit of k = 13 (HNU) or 15 (MSC), all the mapped CAPs were represented in all fMRI sessions of each subject, with significant spatial correlation across sessions ($p < 0.05$, surrogate testing with randomly shuffled cluster associations). At higher partitions, one or more CAPs were instead no longer represented in one or more subjects. We further probed within-session stability of clustering by computing the CAP occurrence rate obtained across imaging sessions. We found that CAP occurrence rate (i.e. proportion of fMRI frames associated to a CAP in each subject), for both datasets, was stable across sessions at k = 2, 6, 8, and 9 (Kruskal-Wallis test, 10 groups for HNU, 5 groups for MSC, FDR corrected for k comparisons, **Figure S2 G-H**).

Finally, to maximize the generalizability of our partitioning, we compared the main dataset's (HNU) CAP maps with those obtained in the MSC in terms of topography matching and occurrence rates. To this aim, we spatially compared mean group-level CAP maps (matched with the Hungarian Algorithm for each partition) and tested the significance of this comparison by recomputing the values after randomly shuffling the fMRI frames within each dataset, while preserving occurrence rates (**Figure S2I**). The mean occurrence rates from each dataset was assessed with a Wilcoxon signed rank test, $p < 0.05$, FDR corrected for k comparisons (**Figure S2J**). This analysis revealed that clusters from all partitions, except k = 6, 7, 9, 14, 15 and 16, were topographically reproducible across datasets (**Figure S2I**). By contrast, a comparison of the mean CAP occurrence rates between datasets (**Figure S2I**) showed that k = 8 was the only partition in which this parameter was

conserved across dataset (Wilcoxon signed rank test, $p < 0.05$, FDR corrected for k comparisons). Based on these analyses, k= 8 was the only partition level meeting all the required within and between subject/dataset reproducibility criteria. We thus based all our subsequent analyses of human fMRI dynamics using k = 8 clusters.

Selection of optimal clusters in macaque fMRI time-series (Newcastle test-retest datasets, n = 8 animals, 2 sessions) followed the same strategy employed for human time-series. Briefly, computation of explained variance in macaque fMRI time-series revealed an elbow region within the k = 6:10 range (**Figure S3A**). Macaque CAPs were topographically stable at increasing k partitions until an upper limit at k = 10 (**Figure S3B**). Comparing repeatability of CAP topographies across sessions revealed that above k = 8, some CAPs present lack of topographical reproducibility ($p > 0.05$, surrogate testing with randomly shuffled cluster associations), as well as significant differences in CAP occurrence rates (Kruskal-Wallis test, FDR corrected for k comparisons, **Figure S3C-D**). This cumulative evidence suggests that k = 8 was the highest partition that guarantees CAP stability, as well as test-retest topographical and frame distribution repeatability amongst clusters.

For mice, the variance explained curve for the awake dataset we used in this work (N = 44) showed an elbow between 6 and 8 clusters (**Figure S3E-F**). Topographic CAP stability as a function of increasing partition number revealed that mouse CAPs were topographically stable up to k = 6. This value is in agreement with the results of CAP number selection in prior independent studies[22,29], in which k = 6 was consistently identified as optimal partition in this species.

Coactivation Modes and between species matching

In previous work we demonstrated that CAPs appear in pairs of spatial configurations with opposite BOLD coactivations[15] (CAP, and anti-CAP, **Figure 1A**). As this feature was initially detected in awake and anesthetized mice[22], we first showed that these anatomical configurations were present also in all of our datasets. For each species, we thus organized CAPs in descending occurrence rate and computed their Pearson's correlation between the vectorized mean CAP maps as a spatial similarity metric, matching CAPs and anti-CAPs as pairs with the highest anticorrelation coefficient (**Figure 1B**). We then reduced pairs into C-modes, by taking each CAP map pair (T-score normalized), subtracting the least recurring one from its counterpart, then dividing the resulting map by two (**Figure 1A**). Given that CAPs represent unique configurations between known resting state networks[15,16,40], we extracted the mean BOLD values from voxels within previously described, evolutionarily conserved[23,42] cortical RSN in humans[20], macaques(Xu et al., 2019a), and mice[22,67]. We also included hippocampal and thalamic masks[53,68] (**Figure 1C**). For each C-mode, we computed their occurrence rates as the average occurrence of the CAP and anti-CAP conforming the C-mode. We then organized the vectorized network coactivation profiles of each C-mode in descending occurrence rate order, and first matched C-mode profiles of humans to macaques, then macaques to mice using the Hungarian Algorithm (**Figure 1D**). We

finally represented the similarities between network coactivation profiles of C-modes in the human HNU dataset and macaques (**Figure 1E**), as well as with the MSC dataset and macaques, confirming our matching (**Figure 1F**). Finally, we matched macaque C-mode network coactivation profiles with those of mice, without accounting for Fronto-Parietal (FPN), Ventral (VAT) and Dorsal Attention (DAT) networks, as these have not been described in the mouse brain (**Figure 1G**). We note that since C-mode 1 was not reliably identified in mice, most likely due to the lack of weighting by higher order VAT, DAT, and FPN, we hereafter exclude C-mode 1 from this species.

After matching and organizing C-modes, the between CAP similarity matrices were plotted, as well as the distributions of C-mode occurrence rates (**Figure 1A-B**). For each species, a comparison of the distributions of occurrence rates was performed (Kruskal-Wallis test, FDR corrected). We then mapped the voxel-wise C-modes as the average between CAP and anti-CAP pairs' T-scores, as well as the z-scored network coactivation profiles within C-modes (voxels' mean +/- SD, **Figure 1C**). Independent group-level CAP maps for each human (HNU and MSC); macaque and mouse dataset are shown in **Figure S4**).

We further tested that in-scanner head-motion did not selectively affect the configuration of any C-mode. This was done by first independently clustering the non- motion censored rsfMRI datasets with k = 8, 8, and 6 for humans, macaques and mice respectively; building C-modes; and then comparing the topographies of matched C-mode maps (Hungarian Algorithm[66]) to the ones obtained after censoring (Pearson's Correlation) (**Figure S5A**). We then computed, for each C-mode in each subject/animal, the proportion of frames in it that were classified as high-head motion (FD > 0.3, 0.3, and 0.075 mm for humans, macaques, and mice, respectively), and compared these distributions across C-modes (one-way ANOVA).

C-mode infraslow dynamics, formation, and temporal structure

We investigated the temporal evolution of C-modes by generating a time-course of instantaneous C-mode to fMRI frame spatial correlation (hereafter referred to as "C-mode time-courses") for each subject/animal, and then computing the power spectrum of these time-courses as well as that of the Global fMRI signal (GS, i.e., the average of all voxels at each frame). We next computed the group mean +/- SEM power spectra. C-mode time-courses were normalized to standard deviation units and mean zero. The evolution of the formation of a C-mode was computed by time-lock averaging the C-mode to frame correlation values at the vicinity of a peak surpassing 1SD (+/- 30 seconds), then averaging these event-kernels at the group level (**Figure 3** insets).

Given that the GS also presented a strong peak in the power spectrum in the [0.01-0.03Hz] infraslow band (**Figure 4A**) we computed whether occurrence of C-modes was phase locked to infraslow GS fluctuations[15,22]. We extracted the instantaneous infraslow phase of the GS (filtered between 0.01-0.03Hz) using the Hilbert Transform, then divided the trace into cycles of minimum 30 s and maximum 100 s. For each cycle, if a C-mode was present, we sampled the GS-phase at

which the C-mode occurred, retaining only samples from normalized C-mode time-courses exceeding 1SD, thus guaranteeing the selection of frames that are reasonably well assigned to a specific C-mode[15]. We then built the distribution of GS-phases from the group-concatenated sampling of C-mode occurrences, and using MATLAB's CircStats toolbox[69], we performed a Rayleigh test ($p < 0.001$, FDR corrected) for deviations from circular uniformity (**Figure 4B**). As in previous our work[15], we also demonstrated that C-modes are phase-locked within GS-cycles by sampling the GS-phase difference between the occurrence of two C-modes within the same GS cycle, or the immediately previous or subsequent one, limiting selection to instances in which C-mode time-courses exceeded 2 standard deviations (**Figure S6**).

To further explore the temporal sequencing of C-mode occurrences and transitions (**Figure 5**), we defined for each dataset, a concatenated sequence of C-mode occurrences across subjects/animals, and calculated the transition probability matrix from a C-mode *i* at time *t* to another C-mode *j* at time *t+1* as the proportion of transitions i-->j and all other transitions from *i*[22,40]. Only transitions within the same subject were included, and we first considered sequences in which we counted the auto-transitions ($i = j$), namely persistence probabilities. Off-diagonal elements ($i \neq j$), named transition probabilities were then computed after building sequences in which we removed the repeating elements in order to control for auto-correlations given the C-mode's dwell time[40,70]. We quantified the directional prevalence of a transition ($P_{ij} > P_{ji}$) by taking their difference. To measure the relative facilitation to reach a C-mode from another, we computed the Entropy of Markov Trajectories (HMT)[22,24] from the off-diagonal matrix elements (i.e. transition probabilities). This method calculates the descriptive complexity of the paths between C-mode (in bits), where a lower complexity refers to less information required to access a destination C-mode *j* from a source C-mode *i*, hence being more accessible as the path travels through less path before reaching its destination. Specifically, for a Markov Chain (MC) defined by transition probability matrix P, we define the Entropy Rate per step $t \rightarrow t + 1$ as:

$$H(MC) = -\sum_{i=1}^{k}\sum_{j=1}^{k} \mu_i P_{ij} \log_2 P_{ij}$$

Where μ is the stationary distribution solving $\mu_j = \sum_i \mu_i P_{ij}$. Also define the Entropy of a Markov Trajectory T_{ij} from C-mode *i* to C-mode *j* as:

$$H(T_{ij}) = K - K' + H_\Delta$$

Where $K = (I - P - M)^{-1}(H^* - H_\Delta)$, *M* is a matrix of stationary probabilities $M_{ij} = \mu_{ij}$; *I* the identity matrix; H^* is the matrix of single-step entropies $H^*_{ij} = H(P_i) = \sum_k \mu_k P_{ik}$ (from C-mode *i* to any C-mode *k*); and H_Δ is a diagonal entropy matrix with trajectories from a C-mode to itself $(H_\Delta)_{ii} = H(MC)/\mu_i$, with zeros if $i \neq j$[24].

Statistical significance of persistence probabilities was tested from random sequences by generating 1000 permutations of C-mode occurrence sequences at the subject/animal level, concatenating the sequences and counting how many times a random iteration exceeded the true value to reach a p-value. Transition probabilities and directional transition prevalence were tested against matrices built after randomly permuting the non-repeating sequences 1000 times at the subject/animal level, concatenating them and removing samples if $Cmode_i(t+1) = Cmode_i(t)$. These surrogates were also used to test the significance of Markov trajectory entropies. To further quantify and assess the relative complexity of transitions to a particular destination C-mode, we quantified, after repeating the analyses with subject level sequences, the sum of the HMT matrix columns, and compared their distributions across C-mode destinations (one-way ANOVA and Tukey test for multiple comparisons, **Fig 5C**).

C-mode influence on static fMRI connectome and functional connectivity gradients

We first generated C-mode co-fluctuation matrices by cross-multiplying the mean C-mode map with itself[32], which yielded a voxel-wise representation of the co-activating (or co-deactivating) peaks of BOLD activity. We then computed the group-level mean Functional Connectivity matrices by computing the Pearson's Correlation between the concatenated time-series of voxels in all subjects/animals in each group[71], and computed the correlation between the vectorized upper triangular part of the FC matrix to the weighted (by occurrence rate) average of the C-mode Co-fluctuation matrices[22] (**Fig S7A-B**). Voxels were ordered according to the RSN they belong to (see **Fig 1C**).

We further explored if the hierarchies that dominate FC are in accordance with the dynamic structure of C-modes. We first computed the gradients of FC matrices from each species using the Diffusion Mapping method (BrainSpace[72] - *diffusion_mapping.m* Matlab function: FC matrix sparse to top 10-percentile per node, 5 components, anisotropic diffusion parameter = 0.5)[67,73]. We mapped the gradients (**Fig S8**) and computed their spatial correlation to the obtained C-modes, matching each C-mode to the gradient with the highest absolute Pearson's correlation (**Fig 6A**). Finally we plotted the variance explained by each gradient (lambda) to the group mean occurrence rate of their matched C-mode, fitting a linear model to this relationship (**Fig 6B**).

ACKNOWLEDGMENTS

This work has received funding from the European Research Council (ERC) under the European Union's Horizon 2020 research and innovation program (#DISCONN; no. 802371 to A.G.). The authors also acknowledge funding from the Simons Foundation (SFARI 982347 to A.G. and S.P).

AUTHOR CONTRIBUTIONS

A.G. and D.G.B. conceived the study. D.G.B., A.G. and T.X. curated and preprocessed the data, and D.G.B. developed the computational analyses with input from A.G., T.X. and S.P.. A.G. and D.G.B. wrote the manuscript with input from T.X., S.P., and B.S.R.

DECLARATION OF INTERESTS

The authors declare no competing interests.

Supplementary Figures

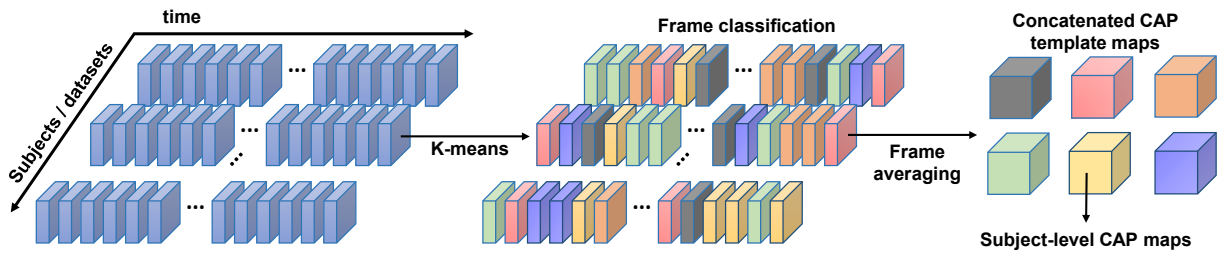

Figure S1. Data clustering and CAP detection (A) fMRI time-series were concatenated and fMRI frames were classified given their spatial similarity (Pearson's Correlation). Frames in a cluster were then averaged at the voxel level to create group-level CAP maps and T-score normalized. Subject-level CAP maps were then computed by averaging fMRI frames for each CAP.

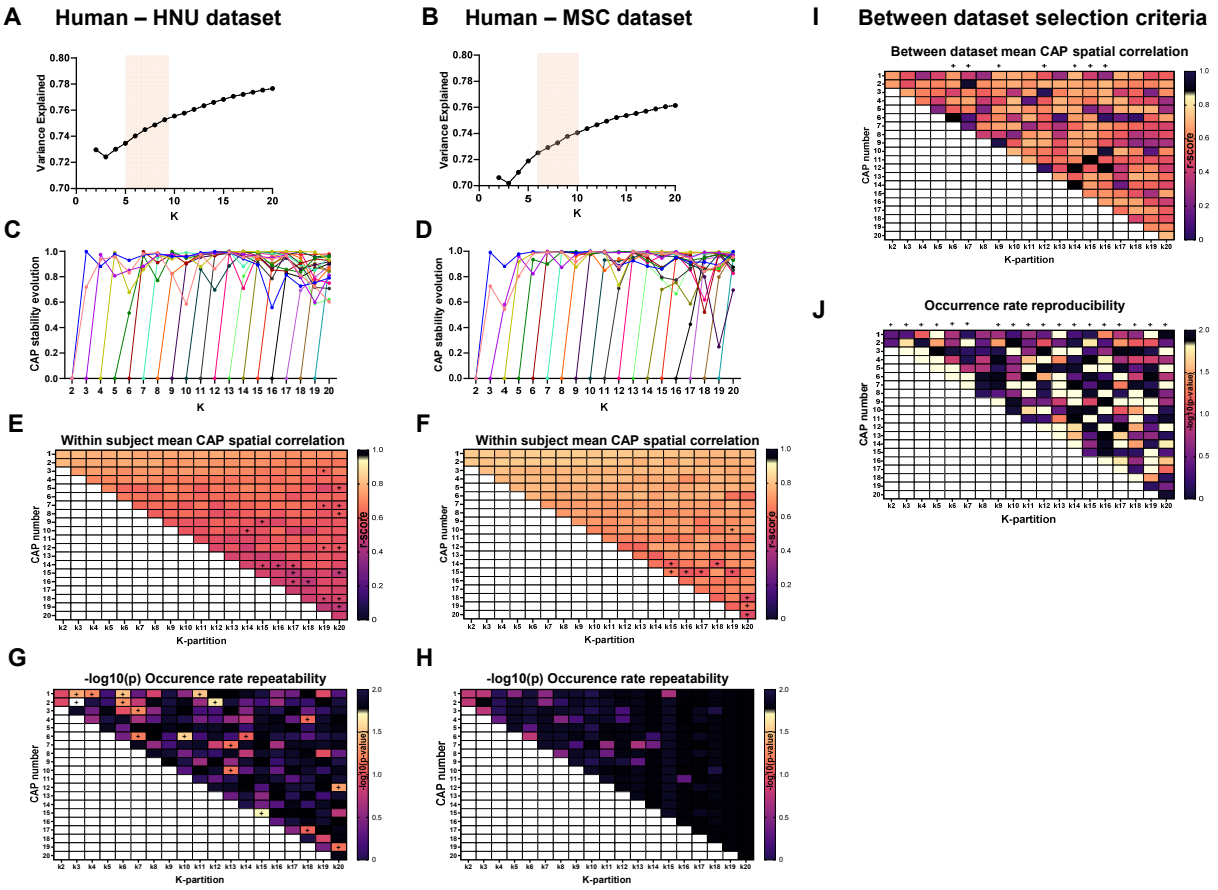

Figure S2. Clustering partition selection – human fMRI time-series. (A-B) Variance explained by clustering each independent dataset (A: HNU, and B: MSC) fMRI frames with k=2:20 (mean +/- SD for 5 runs). **(C-D)** Evolution of CAP stability, i.e, its ability to consistently be detected with the same anatomical configurations at higher partitions. For each partition (k) starting with k=3, the spatial correlation between the matched CAPs from k-1 (Hungarian Algorithm) is plotted, and a the new CAP at zero. **(E-F)** Within subject test-retest repeatability computed as the average spatial correlation between single-subject CAP-maps from all sessions. Asterisks denote CAPs within a partition (k) in which the within-subject correlation values was below a critical value of the highest correlation obtained from 1000 permutations with randomly shuffled fMRI frames, preserving occurrence rate. **(G-H)** Between session occurrence rate repeatability, computed as the –log(10) of the p-value of a Kruskal-Wallis test comparing the medians of all sessions. Asterisks denote CAPs within a partition (k) which showed a significant difference between sessions ($p > 0.05$). **(I)** Between dataset (HNU vs MSC) mean CAP spatial correlations. Asterisks denote partitions (k) in which at least one CAP was not significantly similar between datasets (1000 random permutations of frame reshuffling, preserving CAP occurrence rate). **(J)** Between dataset occurrence rate comparisons. Asterisks denote partitions (k) in which at least one matched CAP had significant differences in the distributions of its occurrence rate (Wilkoxon Signed Rank test, $p < 0.05$, FDR corrected for k comparisons).

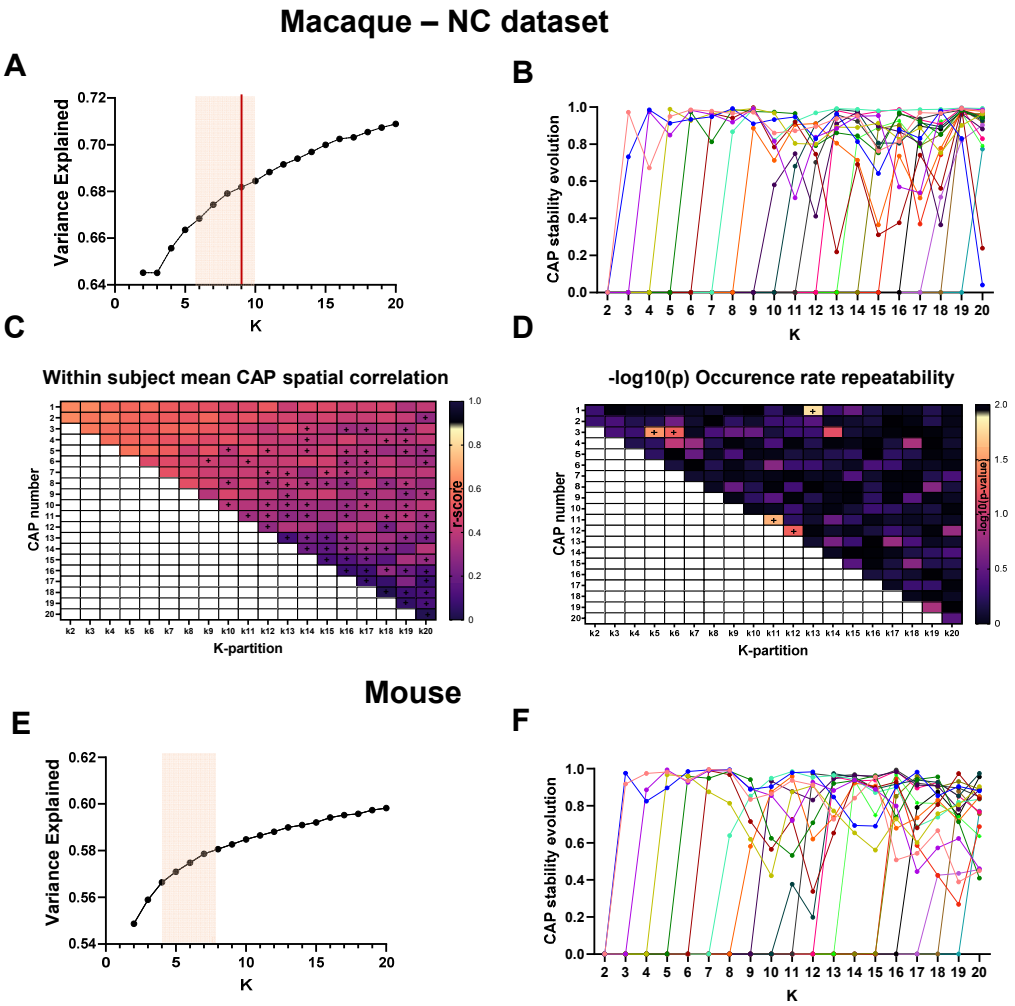

Figure S3. Clustering partition selection –Macaque and mouse fMRI time-series. (A) Variance explained by clustering the concatenated dataset with k=2:20 (mean +/- SD for 5 runs). **(B)** Evolution of CAP stability, i.e., its ability to consistently be detected with the same anatomical configurations at higher partitions. For each partition (k) starting with k=3, the spatial correlation between the matched CAPs from k-1 (Hungarian Algorithm) is plotted, and a the new CAP at zero. **(C)** Within subject test-retest repeatability computed as the average spatial correlation between single-subject CAP-maps from all sessions. Asterisks denote CAPs within a partition (k) in which the within-subject correlation values was below a critical value of the highest correlation obtained from 1000 permutations with randomly shuffled fMRI frames, preserving CAP identity and occurrence rate. **(D)** Between session occurrence rate repeatability, computed as the –log(10) of the p-value of a Wilcoxon Signed Rank test comparing the medians of both sessions. Asterisks denote CAPs within a partition (k) which showed a significant difference between sessions ($p > 0.05$). **(E)** Variance explained by clustering the concatenated mouse dataset with k=2:20 (mean +/- SD for 5 runs). **(F)** Evolution of mice CAP stability, i.e,, its ability to consistently be detected with the same anatomical configurations at higher partitions.

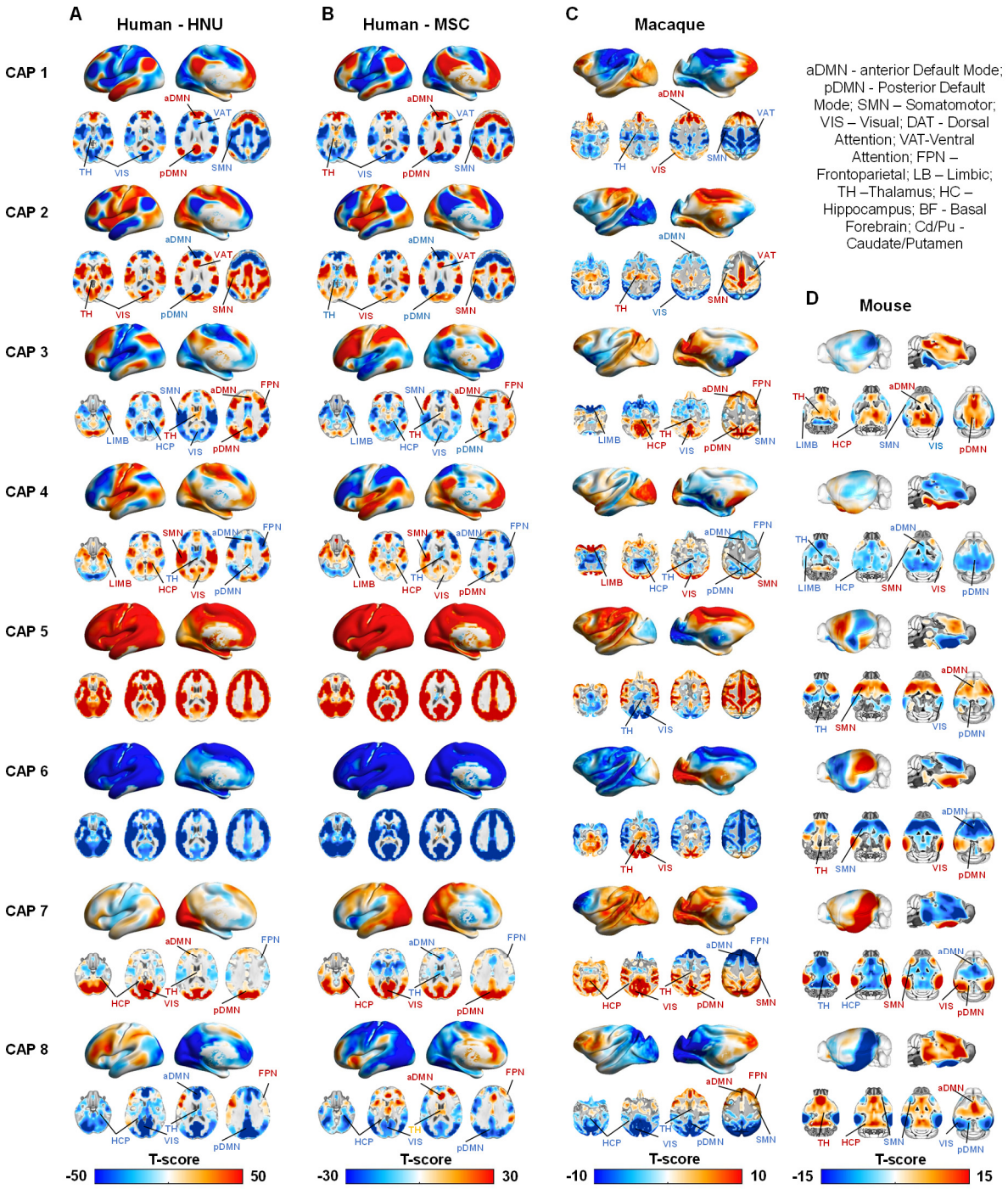

Figure S4. CAPs in awake humans, macaques and mice (A-B) CAPs (T-scores, $p < 0.05$ FDR corrected) of human datasets HNU (A) and MSC (B). **(C)** Macaque CAPs (T-scores, $p < 0.05$ FDR corrected). **(D)** Mouse CAPs (T-scores, $p < 0.05$ FDR corrected). Abbreviations: aDMN - anterior Default Mode; pDMN - Posterior Default Mode; SMN – Somatomotor; VIS – Visual; DAT - Dorsal Attention; VAT-Ventral Attention; FPN – Frontoparietal; LB – Limbic; TH –Thalamus; HC – Hippocampus; BF - Basal Forebrain; Cd/Pu - Caudate/Putamen.

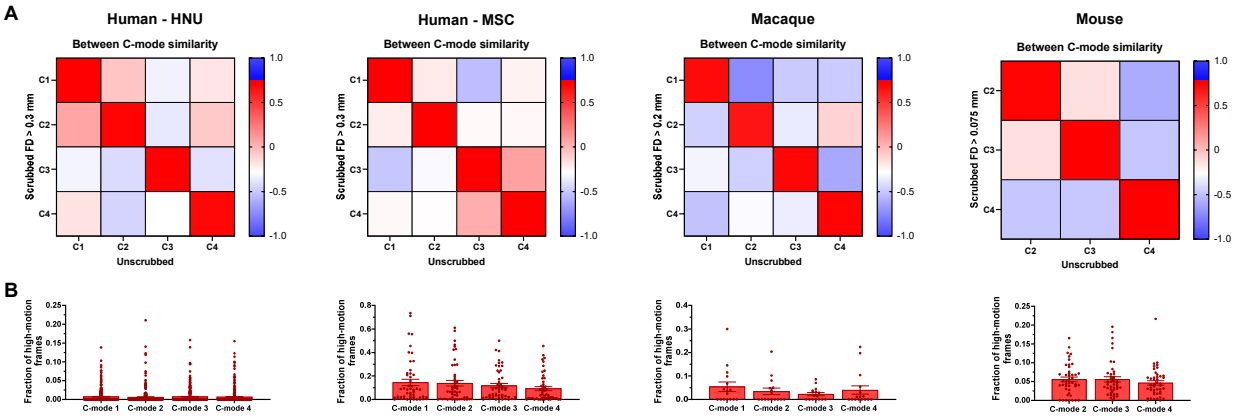

Figure S5. C-modes are not affected by high-motion frames (A) Spatial similarity matrices between C-modes obtained using scrubbed and non-scrubbed data of both human datasets (left), macaques (middle) and mice (right). **(B)** Distribution of the proportion of the fMRI frames within a C-mode that were flagged as high-head motion (FD > 0.3, 0.3, and 0.075 mm for humans, macaques, and mice respectively). No significant differences between C-modes were observed in all species/datasets (one-way ANOVA, $p > 0.1$ for all comparisons, uncorrected).

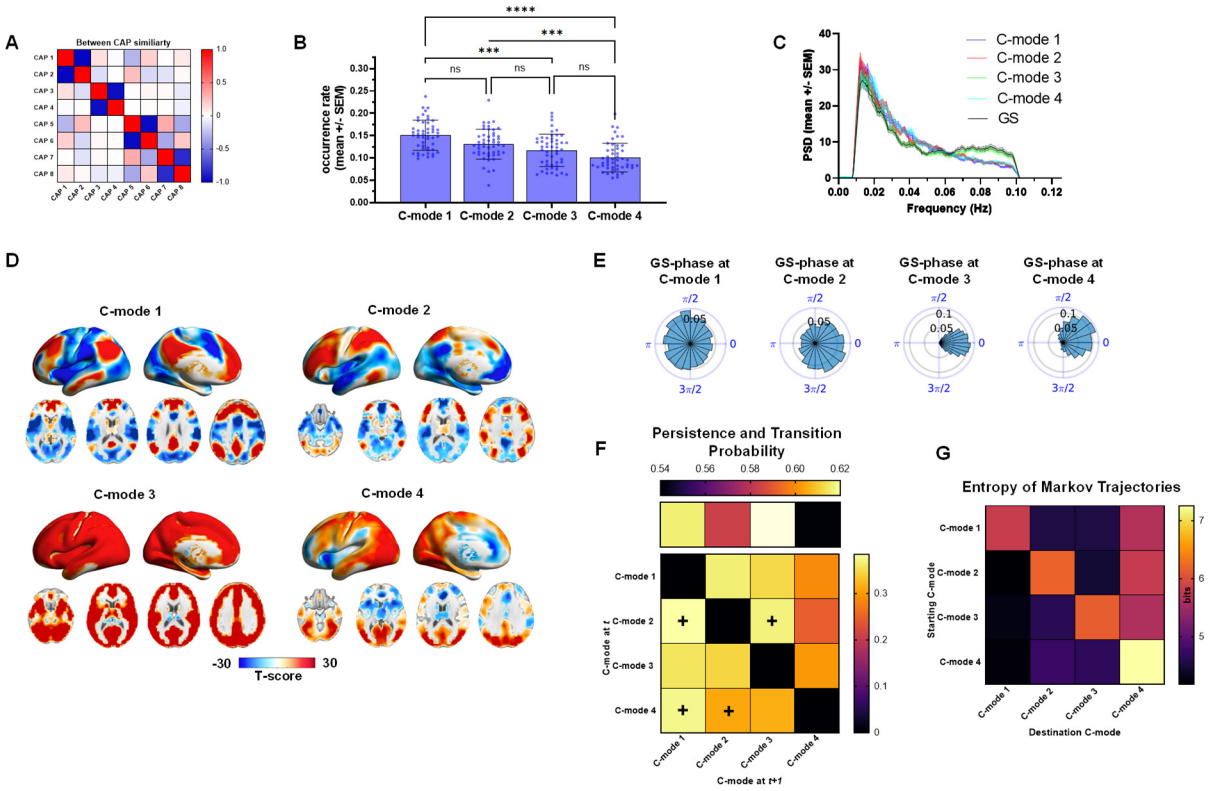

Figure S6. C-modes in MSC dataset reproduce findings from human HNU cohort. (A) Between CAP spatial similarity matrix confirming the existence of CAP-anti-CAP configurations. **(B)** Occurrence rates distributions of C-modes, ordered to their matched C-mode in the HNU dataset using the Hungarian Algorithm. **(C)** Group-level power spectral density (mean +/- SEM) of C-mode time-series, as well as for the Global fMRI Signal (GS). **(C)** C-mode maps from the subtraction of CAP-anti-CAP pairs divided by two. **(E)** GS-phase distributions at the occurrence of each C-mode, conditioned to the C-mode to frame correlation time-course to be > 1SD. All distributions significantly deviate from circular uniformity (Rayleigh test, $p < 0.05$, FDR corrected). **(F)** Persistence (top row) and transition (off-diagonal) probability. Red crosses denote the destination C-mode of preferred directional transitions (Pij > Pji). **(G)** Entropy of Markov trajectories (HMT) show that the C-modes with the highest accessibility are the ones from C-modes with higher occurrence rates. Higher entropy indicates lower accessibility of a destination C-mode (column) from a starting C-mode (row).

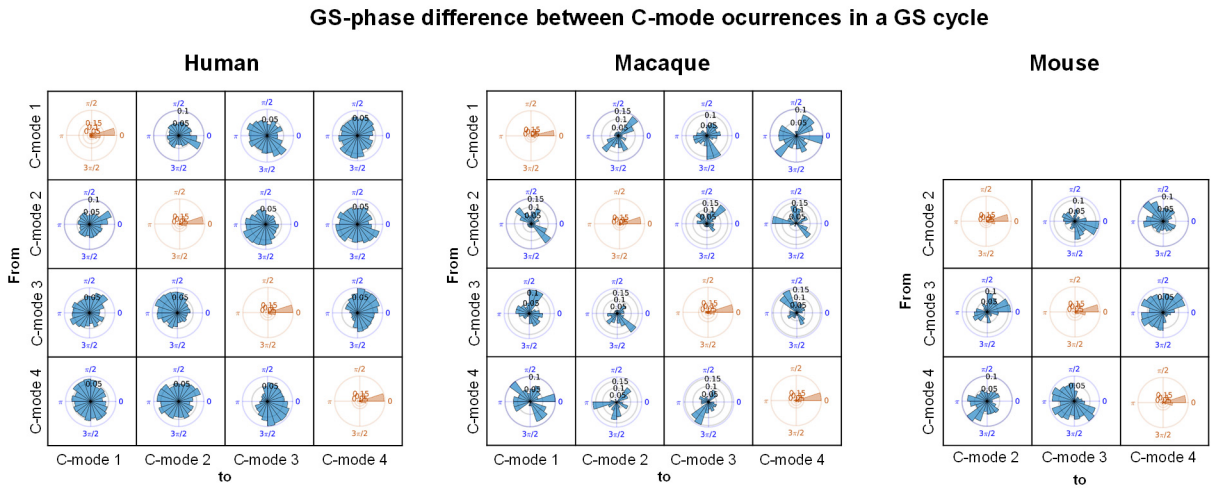

Figure S7. C-mode occurrences are phase-coupled within GS-cycles. Each panel corresponds to the circular distribution of GS phase differences between occurrences of a C-mode within a GS-cycle (rows), and occurrences of another C-mode (columns) within the same cycle or at immediately adjacent cycles. Sampling was conditioned to occurrences in which the C-mode time-course is above 2SD. All distributions significantly deviate from circular uniformity ($p < 0.05$, Rayleigh test).

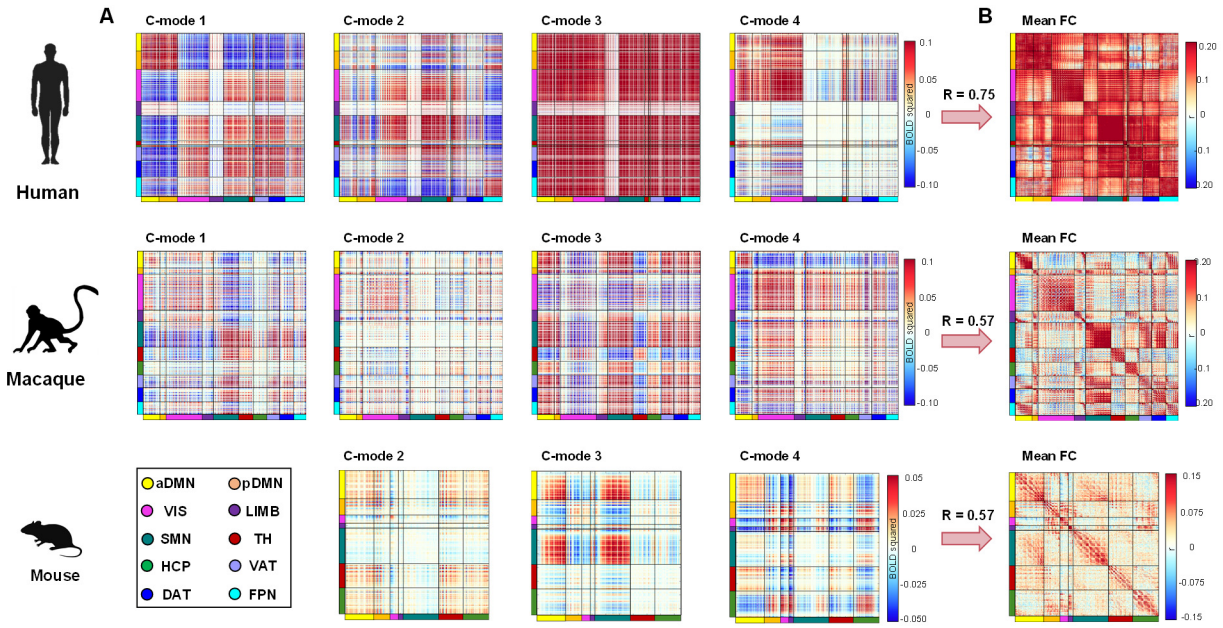

Figure S8. C-Modes topography and occurrence explain functional organization of static fMRI connectome. (A) C-mode Cofluctuation matrices obtain from the tensorial product the each C-mode mean map. **(B)** Group-level voxel-wise Functional Connectivity matrices (Pearson's correlation between concatenated time-series of voxels in all subjects/animals). The black arrow denotes the spatial correlation between vectorized form of the upper-triangular part of the mean FC matrix, and the weighted average of the triangular-parts of the C-modes' cofluctuation matrices (weighted by their average occurrence rates).

Figure S9. Functional Connectivity gradients in awake humans, macaques, and mice. Gradient maps are organized in order of explained connectome variance.

REFERENCES

1. Smith, S. M. *et al.* Correspondence of the brain's functional architecture during activation and rest. *Proc. Natl. Acad. Sci.* **106**, 13040–13045 (2009).

2. Power, J. D. *et al.* Methods to detect, characterize, and remove motion artifact in resting state fMRI. *Neuroimage* **84**, 320–341 (2014).

3. Craddock, R. C. *et al.* Imaging human connectomes at the macroscale. *Nat. Methods* **10**, 524–539 (2013).

4. Gozzi, A. & Zerbi, V. Modeling Brain Dysconnectivity in Rodents. *Biol. Psychiatry* **93**, 419–429 (2023).

5. Milham, M. *et al.* Accelerating the Evolution of Nonhuman Primate Neuroimaging. *Neuron* **105**, 600–603 (2020).

6. Grandjean, J. *et al.* StandardRat: A multi-center consensus protocol to enhance functional connectivity specificity in the rat brain. *bioRxiv* (2022). doi:10.1101/2022.04.27.489658

7. Gozzi, A. & Schwarz, A. J. Large-scale functional connectivity networks in the rodent brain. *Neuroimage* **127**, 496–509 (2016).

8. Tsai, P. J. *et al.* Converging Structural and Functional Evidence for a Rat Salience Network. *Biol. Psychiatry* **88**, 867–878 (2020).

9. Whitesell, J. D. *et al.* Regional, Layer, and Cell-Type-Specific Connectivity of the Mouse Default Mode Network. *Neuron* **109**, 545-559.e8 (2021).

10. Pezzulo, G., Zorzi, M. & Corbetta, M. The secret life of predictive brains: what's spontaneous activity for? *Trends Cogn. Sci.* **25**, 730–743 (2021).

11. Palva, J. M. & Palva, S. Infra-slow fluctuations in electrophysiological recordings, blood-oxygenation-level-dependent signals, and psychophysical time series. *Neuroimage* **62**, 2201–2211 (2012).

12. Preti, M. G., Bolton, T. A. & Van De Ville, D. The dynamic functional connectome: State-of-the-art and perspectives. *Neuroimage* **160**, 41–54 (2017).

13. Lurie, D. J. *et al.* Questions and controversies in the study of time-varying functional connectivity in resting fMRI. *Netw. Neurosci.* **4**, 30–69 (2020).

14. Karahanoğlu, F. I. & Van De Ville, D. Transient brain activity disentangles fMRI resting-state dynamics in terms of spatially and temporally overlapping networks. *Nat. Commun.* **6**, 7751 (2015).

15. Gutierrez-Barragan, D., Basson, M. A., Panzeri, S. & Gozzi, A. Infraslow State Fluctuations Govern Spontaneous fMRI Network Dynamics. *Curr. Biol.* **29**, 2295-2306.e5 (2019).

16. Liu, X., Chang, C. & Duyn, J. H. Decomposition of spontaneous brain activity into distinct fMRI co-activation patterns. *Front. Syst. Neurosci.* **7**, 1–11 (2013).

17. Xu, T. *et al.* Cross-species functional alignment reveals evolutionary hierarchy within the connectome. *Neuroimage* **223**, (2020).

18. Bolt, T. *et al.* A parsimonious description of global functional brain organization in three spatiotemporal patterns. *Nat. Neurosci.* **25**, 1093–1103 (2022).

19. Singleton, S. P. *et al.* Receptor-informed network control theory links LSD and psilocybin to a flattening of the brain's control energy landscape. *Nat. Commun.* **13**, 5812 (2022).

20. Thomas Yeo, B. T. *et al.* The organization of the human cerebral cortex estimated by intrinsic functional connectivity. *J. Neurophysiol.* **106**, 1125–1165 (2011).

21. Xu, T. *et al.* Interindividual Variability of Functional Connectivity in Awake and Anesthetized Rhesus Macaque Monkeys. *Biol. Psychiatry Cogn. Neurosci. Neuroimaging* **4**, 543–553 (2019).

22. Gutierrez-Barragan, D. *et al.* Unique spatiotemporal fMRI dynamics in the awake mouse brain. *Curr. Biol.* **32**, 631-644.e6 (2022).

23. Mars, R. B. *et al.* Whole brain comparative anatomy using connectivity blueprints. *Elife* **7**, 1–15 (2018).

24. Ekroot, L. & Cover, T. M. The entropy of Markov trajectories. *IEEE Trans. Inf. Theory* **39**, 1418–1421 (1993).

25. Esfahlani, F. Z. *et al.* High-amplitude cofluctuations in cortical activity drive functional connectivity. *Proc. Natl. Acad. Sci. U. S. A.* **117**, 28393–28401 (2020).

26. Ragone, E. *et al.* Modular subgraphs in large-scale connectomes underpin spontaneous co-fluctuation "events" in mouse and human brains. *bioRxiv* 2023.05.17.538593 (2023).

27. Margulies, D. S. *et al.* Situating the default-mode network along a principal gradient of macroscale cortical organization. *Proc. Natl. Acad. Sci. U. S. A.* **113**, 12574–12579 (2016).

28. Lu, H. *et al.* Rat brains also have a default mode network. *Proc. Natl. Acad. Sci. U. S. A.* **109**, 3979–3984 (2012).

29. Mandino, F. *et al.* A triple-network organization for the mouse brain. *Mol. Psychiatry* **27**, 865–872 (2022).

30. Pagani, M., Gutierrez-Barragan, D., De Guzman, E. & Gozzi, A. Resting state fMRI connectivity mapping across species: Challenges and opportunities. in *Advances in Resting-State Functional MRI* 21–57 (Elsevier, 2023). doi:10.1016/B978-0-323-91688-2.00009-6

31. Abbas, A. *et al.* Quasi-periodic patterns contribute to functional connectivity in the brain. *Neuroimage* **191**, 193–204 (2019).

32. Faskowitz, J., Esfahlani, F. Z., Jo, Y., Sporns, O. & Betzel, R. F. Edge-centric functional network representations of human cerebral cortex reveal overlapping system-level architecture. *Nat. Neurosci.* **23**, 1644–1654 (2020).

33. Belloy, M. E. *et al.* Resting Brain Fluctuations Are Intrinsically Coupled to Visual Response Dynamics. *Cereb. Cortex* **31**, 1511–1522 (2021).

34. Grandjean, J. *et al.* Dynamic reorganization of intrinsic functional networks in the mouse brain. *Neuroimage* **152**, 497–508 (2017).

35. Ma, Y., Hamilton, C. & Zhang, N. Dynamic Connectivity Patterns in Conscious and Unconscious Brain. *Brain Connect.* **7**, 1–12 (2017).

36. Barttfeld, P. *et al.* Signature of consciousness in the dynamics of resting-state brain activity. *Proc. Natl. Acad. Sci. U. S. A.* **112**, 887–892 (2015).

37. Allen, E. A. *et al.* Tracking whole-brain connectivity dynamics in the resting state. *Cereb. Cortex* **24**, 663–676 (2014).

38. Cabral, J. *et al.* Cognitive performance in healthy older adults relates to spontaneous switching between states of functional connectivity during rest. *Sci. Rep.* **7**, 1–13 (2017).

39. Demertzi, A. *et al.* Human consciousness is supported by dynamic complex patterns of brain signal coordination. *Sci. Adv.* **5**, eaat7603 (2019).

40. Huang, Z., Zhang, J., Wu, J., Mashour, G. A. & Hudetz, A. G. Temporal circuit of macroscale dynamic brain activity supports human consciousness. *Sci. Adv.* **6**, eaaz0087 (2020).

41. Buckner, R. L. & DiNicola, L. M. The brain's default network: updated anatomy, physiology and evolving insights. *Nat. Rev. Neurosci.* **20**, 593–608 (2019).

42. Griffa, A. *et al. The evolution of information transmission in mammalian brain networks*. *bioRxiv* **079**, (2022).

43. Zhang, K. & Sejnowski, T. J. A universal scaling law between gray matter and white matter of cerebral cortex. *Proc. Natl. Acad. Sci. U. S. A.* **97**, 5621–5626 (2000).

44. Ardesch, D. J. *et al.* Scaling Principles of White Matter Connectivity in the Human and Nonhuman Primate Brain. *Cereb. Cortex* **32**, 2831–2842 (2022).

45. Lindstedt, S. L. & Schaeffer, P. J. Use of allometry in predicting anatomical and physiological parameters of mammals. *Lab. Anim.* **36**, 1–19 (2002).

46. Buckner, R. L. & Krienen, F. M. The evolution of distributed association networks in the human brain. *Trends Cogn. Sci.* **17**, 648–665 (2013).

47. Garin, C. M. *et al.* An evolutionary gap in primate default mode network organization. *Cell Rep.* **39**, 110669 (2022).

48. Ville, D. Van De. Brain Dynamics : Global Pulse and Brain State Switching. *Curr. Biol.* **29**, R690–R692 (2019).

49. Liu, X. *et al.* Subcortical evidence for a contribution of arousal to fMRI studies of brain activity. *Nat. Commun.* **9**, 395 (2018).

50. Raut, R. V. *et al.* Global waves synchronize the brain's functional systems with fluctuating arousal. *Sci. Adv.* **7**, eabf2709 (2021).

51. Shine, J. M. *et al.* The Dynamics of Functional Brain Networks: Integrated Network States during Cognitive Task Performance. *Neuron* **92**, 544–554 (2016).

52. Cabral, J., Fernandes, F. F. & Shemesh, N. Intrinsic macroscale oscillatory modes driving long range functional connectivity in female rat brains detected by ultrafast fMRI. *Nat. Commun.* **14**, 375 (2023).

53. Glasser, M. F. *et al.* The minimal preprocessing pipelines for the Human Connectome Project. *Neuroimage* **80**, 105–124 (2013).

54. Cox, R. W. AFNI: Software for analysis and visualization of functional magnetic resonance neuroimages. *Comput. Biomed. Res.* **29**, 162–173 (1996).

55. Jenkinson, M., Beckmann, C. F., Behrens, T. E. J., Woolrich, M. W. & Smith, S. M. FSL - Review. *Neuroimage* **62**, 782–90 (2012).

56. Fischl, B. FreeSurfer. *Neuroimage* **62**, 774–781 (2012).

57. Zuo, X. N. *et al.* An open science resource for establishing reliability and reproducibility in functional connectomics. *Sci. Data* **1**, 1–13 (2014).

58. Gordon, E. M. *et al.* Precision Functional Mapping of Individual Human Brains. *Neuron* **95**, 791-807.e7 (2017).

59. Smith, S. M. Fast robust automated brain extraction. *Hum. Brain Mapp.* **17**, 143–155 (2002).

60. Slater, H. *et al.* Individually customisable non-invasive head immobilisation system for non-human primates with an option for voluntary engagement. *J. Neurosci. Methods* **269**, 46–60 (2016).

61. Milham, M. P. *et al.* An Open Resource for Non-human Primate Imaging. *Neuron* **100**, 61-74.e2 (2018).

62. Donahue, C. J. *et al.* Using diffusion tractography to predict cortical connection strength and distance: A quantitative comparison with tracers in the monkey. *J. Neurosci.* **36**, 6758–6770 (2016).

63. Tustison, N. J. *et al.* Large-scale evaluation of ANTs and FreeSurfer cortical thickness measurements. *Neuroimage* **99**, 166–179 (2014).

64. Craddock, R. C., James, G. A., Holtzheimer, P. E., Hu, X. P. & Mayberg, H. S. A whole brain fMRI atlas generated via spatially constrained spectral clustering. *Hum. Brain Mapp.* **33**, 1914–1928 (2012).

65. Arthur, D. & Vassilvitskii, S. K-Means++: the Advantages of Careful Seeding. *Proc. eighteenth Annu. ACM-SIAM Symp. Discret. algorithms* 1027–1025 (2007). doi:10.1145/1283383.1283494

66. Kuhn, H. W. The Hungarian method for the assignment problem. *Nav. Res. Logist.* **52**, 7–21 (2005).

67. Coletta, L. *et al.* Network structure of the mouse brain connectome with voxel resolution. *Sci. Adv.* **6**, eabb7187 (2020).

68. Hartig, R. *et al.* The Subcortical Atlas of the Rhesus Macaque (SARM) for neuroimaging. *Neuroimage* **235**, (2021).

69. Berens, P. CircStat : A MATLAB Toolbox for Circular Statistics. *J. Stat. Softw.* **31**, 293–295 (2009).

70. Cornblath, E. J. *et al.* Temporal sequences of brain activity at rest are constrained by white matter structure and modulated by cognitive demands. *Commun. Biol.* **3**, 1–12 (2020).

71. Cho, J. W., Korchmaros, A., Vogelstein, J. T., Milham, M. P. & Xu, T. Impact of concatenating fMRI data on reliability for functional connectomics. *Neuroimage* **226**, 117549 (2021).

72. Vos de Wael, R. *et al.* BrainSpace: a toolbox for the analysis of macroscale gradients in neuroimaging and connectomics datasets. *Commun. Biol.* **3**, (2020).

73. Ren, J. *et al.* Individual Variability in Functional Organization of the Human and Monkey Auditory Cortex. *Cereb. Cortex* **31**, 2450–2465 (2021).